Maintenance of cell wall remodeling and vesicle production are connected in *Mycobacterium tuberculosis*

Vivian Salgueiro[1]*, Jorge Bertol[2]*, Claude Gutierrez[3], Ainhoa Palacios[4], Laia Pasquina-Lemonche[5], Akbar Espalliat[6], Laura Lerma[1], Brian Weinrick[7], Jose L. Lavin[8], Felix Elortza[4], Mikel Azkalgorta[4], Alicia Prieto[9], Pilar Buendía-Nacarino[10], José L. Luque-García[10], Olivier Neyrolles[3], Felipe Cava[6], Jamie K. Hobbs[5], Joaquín Sanz[2#] and Rafael Prados-Rosales[1#]

[1]Department of Preventive Medicine and Public Health and Microbiology, Universidad Autónoma de Madrid, Madrid, Spain;[2]Institute for Bio-computation and Physics of Complex Systems BIFI, Department of Theoretical Physics, University of Zaragoza, Zaragoza, Spain; [3]Institut de Pharmacologie et de Biologie Structurale, IPBS, Université de Toulouse, CNRS, UPS, Toulouse, France; [4]CIC bioGUNE, , Basque Research and Technology Alliance (BRTA), Bizkaia Science and Technology Park, Derio, Spain; [5]Department of Physics and Astronomy, University of Sheffield, Sheffield, UK; [6]Department of Molecular Biology and Laboratory for Molecular Infection Medicine Sweden, Umeå Centre for Microbial Research, SciLifeLab, Umeå University, Umeå, Sweden; [7]Trudeau Institute, Saranac Lake, NY, USA; [8]Bioinformatics Unit, Neiker-Tecnalia, Derio, Spain; [9]Department of Microbial & Plan Biotechnology, Centro de Investigaciones Biológicas Margarita Salas, Spanish National Research Council (CSIC),Madrid, Spain; [10]Department of Analytical Chemistry, Universidad Complutense de Madrid, Madrid, Spain.

Key words: extracellular vesicles, *Mycobacterium tuberculosis*, vesiculogenesis, peptidoglycan, membrane, permeability.

#To whom correspondence should be addressed:

Dr. Rafael Prados-Rosales– rafael.prados@uam.es

Dr. Joaquín Sanz- jsanz@bifi.es

*Equal contribution

Running title: *Mycobacterium* vesicle biogenesis mechanism.

Abstract

Pathogenic and nonpathogenic mycobacteria secrete extracellular vesicles under various conditions. EVs produced by *Mycobacterium tuberculosis* (*Mtb*) have raised significant interest for their potential in cell communication, nutrient acquisition, and immune evasion. However, the relevance of vesicle secretion during tuberculosis infection remains unknown due to the limited understanding of mycobacterial vesicle biogenesis. We have previously shown that a transposon mutant in the LCP-related gene *virR* (*virR*^{mut}) manifested a strong attenuated phenotype during experimental macrophage and murine infections, concomitant to an enhanced vesicle release phenotype. In this study, we aimed to understand the role of VirR in the vesicle production process in *Mtb*. We employ genetic, transcriptional, proteomics, ultrastructural and biochemical methods to investigate the underlying processes explaining the enhanced vesiculogenesis phenomenon observed in the *virR* mutant. Our results establish that VirR is critical to sustain proper cell permeability via regulation of cell envelope remodeling possibly through the interaction with similar cell envelope proteins, which control the link between peptidoglycan and arabinogalactan. These findings advance our understanding of mycobacterial extracellular vesicle biogenesis and suggest that these set of proteins could be attractive targets for therapeutic intervention.

Introduction

Mycobacterium tuberculosis (*Mtb*) is one of the most successful human pathogens with the capacity to persist within the host establishing long-lasting infections. *Mtb* possesses multiple highly evolved mechanisms to manipulate host cellular machinery and evade the host immune system. Similar to other intracellular pathogens, *Mtb* releases proteins and lipids, that interfere with host cellular processes, via canonical or specialized secretion systems (Majlessi et al., 2015). How mycobacteria confined within phagosomes delivers virulence factors to other cellular compartments and/or into the extracellular milieu to affect the physiology of neighboring cells is currently a matter of investigation. Understanding the physiology of this phenomenon during the infection process might be critical to develop alternative therapies against tuberculosis (TB).

Like most forms of life, *Mtb* uses an alternative antigen release process based on extracellular vesicles (EVs) (R Prados-Rosales et al., 2011). Mycobacterial EVs (MEVs) are membrane walled spheres of 60-300 nm in diameter, released by live bacteria *in vitro* and *in vivo*. MEVs contain iron scavenging molecules, immunologically active complex lipids and lipoproteins, and classical virulence factors such as the *Mycobacterium ulcerans* toxin mycolactone (Lee et al., 2015; Marsollier et al., 2007; R Prados-Rosales et al., 2011; Prados-Rosales et al., 2014b). Several studies have clearly established a role of MEVs in immunomodulation and shown that MEVs deliver factors that impair macrophage effector functions, inhibit T cell activation, and modify the response of host cells to infection (Athman et al., 2015, 2017; R Prados-Rosales et al., 2011; Prados-Rosales et al., 2014b, 2014a; Rath et al., 2013). MEVs have also shown potential as biomarkers of *Mtb* infection (Schirmer et al., 2022; Ziegenbalg et al., 2013). Although the importance of MEVs has been recognized, hardly anything is known regarding both how such vesicles are exported across the mycobacterial cell wall and the molecular mechanisms underlying vesicle formation in mycobacteria. To date, several modulators of MEVs have been described. Our group identified two conditions leading to stimulation of vesicle production, namely: iron starvation (Prados-Rosales et al., 2014b) and the deletion of *virR* (Rv0431, vesiculogenesis and immune response Regulator) (Rath et al., 2013). In addition, it was shown that the Pst/SenX3-RegX3 signal transduction system regulates MEVs production independent from VirR (White et al., 2018), suggesting an alternative mechanism of vesicle production. We have recently demonstrated that both iron starvation and deletion of VirR in *Mtb*, two hypervesiculating conditions, trigger the induction of the isoniazid-induced gene operon *iniBAC* (Gupta et al., 2023). We determined that both IniA and IniC are dynamin-like proteins (DLP) presumably assisting MEV release through the fusion of the cell membrane (Gupta et al., 2023; Wang et al.,

124 2019). Understanding how defects in VirR lead to hypervesiculation through DLPs is
125 important to provide mechanistic explanation for the vesiculation process in
126 mycobacteria.

127 Several lines of evidence support the notion that VirR might be involved in
128 maintaining cell wall integrity: (i) First, sequence analysis of the VirR protein indicates
129 that it contains a conserved LytR_C domain (**Fig S1**), which is usually found in
130 combination with another domain named LytR-Cps2A-Psr (LCP), and proteins carrying
131 both domains have been associated with the remodeling of the cell wall in Gram-positive
132 bacteria (Hubscher et al., 2008). *Mtb* has six genes encoding for LCP proteins, three with
133 both LCP and LytR_C domains (Rv3267, Rv3484 and Rv0822), two with a solo LytR_C
134 domain (VirR and Rv2700) and one protein with a solo LCP domain (Rv3840) (**Fig S1**).
135 The LCP family includes enzymes that transfer glycopolymers from membrane-linked
136 precursors to peptidoglycan (PG) or cell envelope proteins and are central to cell
137 envelope integrity (Kawai et al., 2011). In mycobacteria its was demonstrated that some
138 members of the (LCP) family of proteins are responsible for the linkage between
139 arabinogalactan (AG) and PG (Grzegorzewicz et al., 2016; Harrison et al., 2016).
140 Rv3267, Rv3484 and Rv0822 appear to have overlapping functions in cell wall assembly,
141 Rv3267 being the primary ligase (Grzegorzewicz et al., 2016). Interestingly, while
142 knocking down the gene encoding for the main AG-PG ligase (cg0847, LcpA) in
143 *Corynebacterium glutamicum* leads to the release of outer membrane material to the
144 extracellular medium (Baumgart et al., 2016), this phenotype is not observed in any
145 knockout strain in the *Mtb* orthologs (Grzegorzewicz et al., 2016), probably reflecting the
146 ability of the mutants to negatively regulate the biosynthesis of cell wall constituents in
147 response to a decrease in ligase activity; (ii) Second, we and others have determined
148 the increased susceptibility of the transposon *virR* mutant (*virR*^{mut}) with respect to the
149 WT (Ballister et al., 2019; Rath et al., 2013), and the mutant in the *virR* ortholog, Rv2700
150 (cell envelope integrity, *cei*) to cell wall targeting drugs such as meropenem (Ballister et
151 al., 2019). Based on these results, we hypothesize that LytR_C solo domain proteins
152 including VirR and cei (Rv2700) have critical roles in the maintenance of cell wall
153 homeostasis and their absence leads to cell wall alterations leading to enhanced
154 vesiculation.

155 In this work we show that the absence of VirR leads to ultrastructural changes in
156 the cell envelope as observed by cryo-electron microscopy (cryo-EM). These changes
157 are compatible with enhanced permeability and an enlargement of the PG layer, as
158 measured by high resolution atomic force microscopy (AFM). We demonstrate that VirR
159 interacts with canonical LCP proteins and propose a model for such interaction. These
160 results indicate that VirR is a central scaffold at the cell envelope remodeling process

161 assisting the PG-AG linking process and that this function is important for vesicle
162 production in *Mtb*.
163
164
165 ## Results
166
167 **High EV production linked to the lack of VirR is associated with an altered cell**
168 **envelope in *Mtb* in the absence of cell lysis.** While Gram-negative bacteria can
169 release outer membrane vesicles directly into the extracellular environment from their
170 outermost compartment, Gram-positive bacteria and mycobacteria have thick cell
171 envelopes surrounding the cytoplasmic membrane that acts as a permeability barrier.
172 The mycobacterial cell envelope is composed of PG covalently linked to AG, which in
173 turn is decorated with exceptionally long-chain mycolic acids (MA). These MA, together
174 with intercalating glycolipids, form the unique mycobacterial outer membrane (OM)
175 (Kalscheuer et al., 2019). Previous analysis of mycobacterial vesicle associated lipids
176 showed predominantly polar lipids, consistent with the cytoplasmic membrane being the
177 likely origin of the vesicles (R Prados-Rosales et al., 2011). This is also true in EV
178 produced by Fe-limited *Mtb* whose lipid content consists mainly of polar lipids and the
179 lipidic siderophore, mycobactin (Prados-Rosales et al., 2014b). Given that these vesicles
180 must traffic from their point of origin in the plasma membrane through the cell envelope,
181 we hypothesized that local remodeling of the cell envelope is necessary for EV release,
182 and that this process may be exacerbated in a *virR* mutant (*virR*^{mut}). To test this, we
183 examined the cell envelope structure of *virR*^{mut} grown in minimal medium (MM), as well
184 as wild type (WT) and *virR*^{mut} complemented (*virR*^{mut}-C) strains (Rath et al., 2013) (**Fig**
185 **1**). Using cryo-EM on whole cells, which allows the study of mycobacterial cell surface-
186 associated compartments in a close-to-native state (Sani et al., 2010), we could easily
187 discern three layers comprising the mycobacterial cell envelope: i) the outer membrane
188 (OM); ii) an intermediate layer composed of two sublayers (L1 and L2, previously
189 assigned to the mycolate-PG-AG (mAGP) network (Sani et al., 2010)); and iii) the
190 cytoplasmic membrane (CM) (**Fig 1**). We observed a significant increase in the thickness
191 of the overall cell envelope (OM-CM) in the *virR*^{mut} strain compared to the WT. This
192 difference was largely explained by the expansion of the CM-L1 layer suggesting cell
193 wall alterations closer to the cell membrane and indicating aberrant production of either
194 AG, PG or both. Complementation with a functional copy of *virR* restored normal cell
195 envelope structure (**Fig 1A-C**).
196 In Gram-negative bacteria increased vesiculation has been observed in conditions
197 associated with either loss or maintenance of periplasm integrity (McMillan and Kuehn,

198 2021). Moreover, a novel mechanism of vesicle production common to both Gram-
199 negative and Gram-positive bacteria has recently been described, in which a cell
200 explosion phenomenon driven by bacteriophages leads to the formation of EVs in culture
201 when bacteria are under genotoxic stress (Nagakubo et al., 2021). Consequently, we
202 tested whether the enhanced vesiculation described in *virR*^{mut} (Rath et al., 2013) could
203 be linked to cell lysis events. To do this, we analyzed the presence of cytoplasmic IdeR,
204 a transcription factor which is not present in EVs and is not detected in secreted proteins
205 preparations, in culture supernatants of *Mtb* strains, assuming that its detection could be
206 linked to a loss of envelope integrity (Gupta et al., 2023). We first confirmed that the
207 *virR*^{mut} strain manifested an enhanced vesiculation by measuring EVs using nanoparticle
208 tracking analysis (NTA) (**Fig S2A**). We did not detect differences in size distribution of
209 isolated EVs between strains. The same supernatants and cell lysates were used to
210 detect the presence of IdeR by immunoblot using a specific polyclonal antibody (Pandey
211 and Rodriguez, 2014). As a control for normal release of an extracellular protein, we
212 used a monoclonal antibody against Ag85b (Prados-Rosales et al., 2017). We could not
213 detect IdeR in the supernatant of any of the strains, indicating that defects of *virR* do not
214 lead to cell lysis (**Fig S2B**). Taken together, the observed changes in the cell envelope
215 of high EV producing bacteria suggest that cell envelope alterations in response to lack
216 of VirR and increased membrane vesicle biogenesis may be connected in *Mtb*.
217
218 **The absence of LytR_C solo domain proteins in *Mtb* leads to enhanced cell**
219 **envelope permeability concomitant to hypervesiculation.** The collective cryoEM
220 observations that indicated an enlargement of the compartment next to the cell
221 membrane may be linked to a more permeable cell envelope. Supporting this notion is
222 the recent finding that *virR*^{mut} or the mutant in the *virR* ortholog *cei* (Rv2700) manifest
223 an enhanced uptake of ethidium bromide (EtBr) relative to WT strain (Ballister et al.,
224 2019). We could reproduce these results and add that *virR*^{mut}-C strain restores the
225 permeability levels of the WT strain (**Fig 2A**). This enhanced permeability was
226 concomitant to an increased sensitivity to different antitubercular drugs, including
227 meropenem and vancomycin (Ballister et al., 2019). In agreement with these results, we
228 could measure a significantly enhanced sensitivity of *virR*^{mut} to the PG-targeting drug
229 vancomycin relative to WT and *virR*^{mut}-C strains (**Fig 2B**). Interestingly, the magnitude of
230 the sensitivity to cell wall targeting drugs was either moderate (ethambutol) or absent
231 (isoniazid) in *virR*^{mut} (Ballister et al., 2019). Furthermore, we observed enhanced
232 incorporation of fluorescent D-amino acids (FDAAs) in *virR*^{mut} relative to the WT strain in
233 both MM and 7H9 media (**Fig 2C**), again suggesting increased permeability, altered PG
234 turnover or both.

235 We then tested whether the enhanced permeability and vesiculation of *virR*^{mut} are also
236 connected in an *Mtb* mutant lacking Cei (Ballister et al., 2019). To do this, we generated
237 *cei* conditional mutants using the CRISPR interference (CRISPRi) technology (Rock et
238 al., 2017). Further, we also generated *virR* CRISPRi conditional mutants to properly
239 compare both strains (**Fig 2D**). When these strains were cultured in the presence of
240 anhydrotetracycline (ATc) to induce the transcriptional silencing of target genes, we
241 could measure enhanced vesiculation by analyzing vesicle concentration in the
242 supernatant by NTA (**Fig 2E**), relative to strains cultured in the absence of ATc. Overall,
243 these results validate the enhanced permeability phenotype of *Mtb* mutants in the
244 LytR_C solo domain proteins VirR and Cei and establish that this subfamily of proteins
245 participates in the regulation of vesicle production in *Mtb*. Moreover, the higher
246 susceptibility to PG-cross-linking inhibitors in both mutants and the enhanced
247 incorporation of FDAAs in the *virR* mutant strain suggests defects in PG remodeling.
248
249 **Transcriptional profiling of *virR*^{mut} showcases systemic alterations in cell wall**
250 **architecture and metabolism.** To identify VirR-dependent mediators of vesicle
251 production, we carried out a transcriptional profiling of *virR*^{mut} and compared it to that of
252 WT strain. Previous efforts to define the transcriptional profile of *virR*^{mut} showed no
253 significant differences compared to WT (Rath et al., 2013). However, those experiments
254 were carried out with bacteria grown in rich 7H9 medium, while here, we use a defined
255 high-Fe minimal medium (MM), which is typically used for vesiculation experiments (R
256 Prados-Rosales et al., 2011). We extracted RNA from four independent cultures
257 (average optical densities (OD) of 0.4 and 0.38 for WT and *virR*^{mut}, respectively) one day
258 before vesicle isolation and conducted RNA-seq. Of these, N=3 and N=4 libraries of WT
259 and *virR*^{mut} passed QC (**Fig 3A**). Principal component analysis (PCA) was then
260 performed on the transcriptomic data, after filtering out lowly expressed genes, as well
261 as genes containing outlier observations (N=4004 genes tested), and revealed
262 significant differences between strains, aligned with the first principal component (**Fig**
263 **3B**, one-tailed Mann-Whitney test p=2.86e-02), explaining as much as 78.27% of total
264 gene expression variance. We then conducted differential expression analysis to find
265 1663 genes differentially expressed in *virR*^{mut} compared to WT (**Fig 3C**, Benjamini-
266 Hochberg FDR<0.05), which represent 41.5% of all genes tested.
267 Next, we looked for gene ontologies enriched among these VirR-dependent
268 genes, stratified by the direction of the effects (750 up-regulated, and 913 down-
269 regulated in *virR*^{mut} relative to WT). The enrichment analyses highlighted five main
270 groups of biological processes and cell compartment ontologies that appeared altered in
271 *virR*^{mut} with respect to WT (**Fig 3D**). First, among genes that were expressed at lower

272 levels in *virR*^{mut}, we found enrichments terms related to several stress associated with
273 the intra-phagosomal environment (Schnappinger et al., 2003), such as response to
274 hypoxia (FDR=1.14e-06), heat (FDR = 4.24 e-03) or oxidative stress (response to
275 reactive oxygen species: FDR=9.00e-02), suggesting that responses to host-induced
276 stress are compromised in the mutant, as it is also suggested by the enrichment of
277 responses to host immune response (FDR=2.00 e-02). Furthermore, the mutant strain
278 showed a reduction in transcripts related to the protein secretion term (FDR=2.51e-04),
279 and, specifically, protein secretion by the type VII secretion system (FDR=1.15 e-04).
280 Contributing to this enrichment, we found that both components of the key antigen-dimer
281 ESAT-6/Cfp10, (Rv3875 and Rv3874, respectively), were significantly downregulated in
282 the mutant strain (log2FC =-0.15, FDR=1.94 e-02 for Rv3875, and log2FC= -0.16, FDR
283 = 2.25 e-02 for Rv3874).
284 Second, we found terms related to lipid metabolism and transport: (e.g. fatty acid
285 biosynthetic process: FDR=4.92e-02; steroid metabolism, FDR=4.24e-03) enriched
286 among downregulated genes in *virR*^{mut}, suggesting that the regulation of both anabolic
287 and catabolic pathways of lipids, key for bacterial survival and pathogenesis upon
288 infection (Ghazaei, 2018), are partially VirR-dependent. However, not every lipid-related
289 pathway appeared downregulated in the mutant strain, since PDIM biosynthesis genes
290 were predominantly up-regulated in the mutant (DIM/DIP cell wall layer assembly
291 enrichment FDR=3.60e-02, and phenolic phtiocerol biosynthetic process FDR=3.60e-
292 02).
293 The third group of enrichments included terms related to global regulation of gene
294 expression, mostly enriched among downregulated genes in *virR*^{mut} (positive regulation
295 of gene expression FDR=1.82 e-02, positive regulation of transcription, DNA templated
296 FDR=4.92 e-02), suggesting a global alteration of the transcriptional landscape. The
297 remaining two groups of ontologies included terms related to energy-production
298 metabolism and post-transcriptional regulatory processes and compartments. Among
299 these terms, we found evidence for an enrichment of genes encoding ribosome-located
300 proteins (large ribosomal subunit, FDR= 3.60e-02) among genes up-regulated in *virR*^{mut},
301 which suggests the involvement of relevant VirR-dependent post-transcriptional
302 regulatory processes impacting protein biosynthesis in the mutant. Similarly,
303 enrichments of further key metabolic pathways beyond lipids metabolic routes included
304 terms enriched among genes down-regulated in *virR*^{mut}, such as electron transport chain,
305 (FDR=9.15 e-03), and ATP biosynthetic process (FDR=1.36 e-02), as well as terms
306 enriched among upregulated genes in the mutant such as NADH dehydrogenase activity,
307 (FDR=1.53 e-02). All together, these results combined with the differences concerning

308 lipid metabolism discussed above, suggest a global remodeling of metabolic networks in
309 *virR*^{mut}.
310
311 ***virR* regulates the protein content of EVs in *Mtb***. To capture the impact of
312 transcriptional adaptation to the proteome and the degree of divergence between
313 transcriptional shifts and proteins changes of *Mtb* in the absence of *virR*, we next
314 performed label-free peptide mass spectrometry (LF-MS) of whole cell lysates (WCLs)
315 of *virR*^{mut} and WT strains. Additionally, we isolated EVs from axenic cultures and
316 obtained their proteomic composition to examine for potential VirR-dependent
317 differences in protein cargo that may alter the functionality of EVs (**Fig 4A**). As a result,
318 we obtained proteomic profiles across strains and cell compartments for a total of N=934
319 proteins. Upon PCA analysis of the proteomic data (**Fig 4B**), we found that the first
320 principal component (PC1), explaining 36.8% of total variance, separated samples from
321 WCLs and EVs regardless of the strain (PC1 differs across cell compartments: one-tailed
322 Mann Whitney t test p=1.08e-03), while the second PC (PC2) (21.3% of total variance
323 explained) captured strain effects on the proteomic footprint only among EVs (one-tailed
324 Mann Whitney t test for PC2 differences between *virR*^{mut} EVs and the rest: p=4.55 e-03).
325 These results suggest that differences in protein abundances between EVs and WCLs
326 are larger than differences found between strains, and that, concerning the differences
327 across strains, these are comparatively more important in EVs. Next, we conducted
328 differential protein expression analyses to find 15 upregulated and 4 downregulated
329 proteins between WT and *virR*^{mut} strains in WCLs, at FDR=5%, which represents 2% of
330 the total of proteins under analyses (**Fig 4C, right bar**). Despite the scarcity of significant
331 differences in expression across strains in WCLs, some of the proteins most differentially
332 expressed in *virR*^{mut} are involved in key processes for bacterial survival and virulence,
333 including key metabolic enzymes such as the Acetyl-coenzyme A synthetase AcsA
334 (logFC = -3.78, FDR = 4.40 e-03), as well as FprA, (logFC= -2.77, FDR=1.55 e-02),
335 involved in the reduction of NADP+ into NADPH, both downregulated in *virR*^{mut}.
336 Conversely to the WCL dataset, we did find larger differences in protein
337 expression across strains in EVs, with 187 proteins more abundant and 166 less
338 abundant in *virR*^{mut} EVs than that of WT (**Fig 4C, left bar**). This represents 37.8% of all
339 proteins tested, a value largely comparable to the percentage of differentially expressed
340 genes identified in the RNA-seq data. Regarding downregulated EV proteins in *virR*^{mut}
341 we observed robust enrichments in ontology terms related with protein biosynthesis,
342 including translation (FDR=2.09 e-28), ribosome (FDR=3.01 e-37), and ribosome
343 assembly (FDR=6.71 e-04), indicating that EVs from the *virR*^{mut} are ribosome-depleted.
344 Consistent with these results 42 ribosomal proteins were found to be less abundant in

345 the *virR*^{mut} strain relative to WT (**Fig S3**). Interestingly, these results contrast with the
346 higher mRNA levels found for genes associated with the ribosomal compartment in the
347 RNA-seq data obtained from WCLs (**Fig 3D**, **right panel**), suggesting that the depletion
348 of ribosomal content found in the vesicles is the result of post-transcriptional regulatory
349 events. Furthermore, we found that the two bacterioferritin proteins BfrA (log2FC=-3.19,
350 FDR=3.42 e-04) and BfrB (log2FC=-2.47, FDR=9.70 e-05), were simultaneously less
351 abundant in *virR*^{mut}, (**Fig 4E**), together contributing to the enrichment of the ontology term
352 ferroxidase activity (FDR=8.30 e-02) (**Fig 4D**). This result is suggestive of a possible
353 defect of *virR*^{mut} EVs in iron sequestration (Mohammadzadeh et al., 2021; Prados-
354 Rosales et al., 2014b). We also found differences in metabolic pathways associated to
355 the EV content, including enzymes involved in metabolism of nucleotides (FDR=9.63e-
356 02 (up), (FDR=8.30e-02 (down), cellular amino acids ((FDR=6.26e-04 (up), FDR=1.41e-
357 02 (down)) as well as carbohydrates (glycogen FDR=9.63e-02 (up), oligosaccharides
358 FDR=8.30e-02 (down)). The simultaneous enrichments of these metabolic pathways
359 observed both among upregulated and downregulated vesicular proteins (**Fig S4**),
360 indicates a complex, VirR-dependent, rewiring of metabolic routes in the vesicles from
361 the mutant strain.
362 Further, proteins upregulated in *virR*^{mut} EVs were enriched in terms related to
363 mycolic acid metabolism (FDR=1.10 e-03), and peptidoglycan-based cell-wall
364 biogenesis (FDR=1.44 e-02). Proteins such as InhA (logFC=3.65 FDR=6.10 e-05), and
365 KasB (logFC=1.78 FDR=1.22 e-02), involved in mycolic acid synthesis were also
366 upregulated in *virR*^{mut} (**Fig 4F**). The upregulation of these proteins, along with the
367 enrichments at the transcriptional level of DIM/DIP biosynthetic pathways (upregulated
368 in *virR*^{mut}), as well as steroid catabolic routes (down-regulated), suggests a shift in the
369 control of the pool of propionyl-CoA, both at the level of its production, -as a byproduct
370 of the catabolism of methyl-branched lipids, odd-chain-length fatty acids as well as
371 cholesterol- and its detoxification by the bacterium through different routes, such as the
372 methylmalonyl pathway, the glyoxylate cycle and the methylcitrate cycles (Lee et al.,
373 2013). To shed light on these changes at the metabolic level, we conducted a metabolic
374 profiling to quantify the concentration of metabolites that are central in these different
375 detoxification routes including propionyl-CoA: acetyl-CoA, pyruvate, methylcitrate, and
376 methylmalonyl-CoA (**Fig 4G, left bottom panel**). Only methylmalonyl-CoA was found to
377 be significantly repressed in *virR*^{mut} (p=0.028). This result, along with the trend towards
378 increased protein, and especially gene expression that is observed for genes involved in
379 the biosynthesis of PDIMs from methylmalonyl (including phenolpthiocerol synthesis
380 type-I polyketide synthases A-E, (ppsA-E), fatty-acid-CoA synthetases fadD26 and
381 fadD28, among others, **Fig 4G**), suggests that the methylmalonyl pool is depleted in the

382 mutant strain as a result of an increased activity of the PDIM biosynthetic pathway.
383 Furthermore, the acetyl/propionyl-CoA carboxylase subunits Acc, appear repressed in
384 *virR*^{mut} EVs, suggesting that the production of methylmalonyl Co-A from the degradation
385 of propionyl CoA is inhibited within the vesicles of the mutant strain.
386 Taken together, the omics analyses align with the structural and functional
387 differences observed in *virR*^{mut}. We reasoned that the increased expression of PDIMs
388 biosynthetic genes and the reduced expression of genes related to protein synthesis may
389 be triggered to compensate the enhanced permeability measured in *virR*^{mut}. In addition,
390 this enhanced permeability leads to an increase in the release of EV, which seems to be
391 depleted in ribosomes and iron storage proteins.
392
393 **Cell envelope permeability is a major driver of MEV release**. If enhanced cell
394 permeability is a global consequence of *virR* disruption that leads to enhanced
395 vesiculation, we hypothesized that other conditions either inducing or decreasing cell
396 envelope permeability could lead to alterations in vesicle production in *Mtb*. To test this,
397 we treated *Mtb* with sublethal concentrations of thioridazine (TRZ), a known enhancer of
398 cell permeability (De Keijzer et al., 2016); and, alternatively, we cultured the bacillus with
399 cholesterol as a sole carbon source, a condition which reduces mycobacterial cell
400 permeability (Brzostek et al., 2009) (**Fig 5A**). Neither condition altered bacterial viability
401 as measured by the absence of the release of the transcription factor IdeR, as an
402 indication of cell lysis (**Fig S2C**). We then measured vesicle levels in culture
403 supernatants and found that *Mtb* significantly releases more vesicles upon treatment with
404 TRZ, and significantly reduces vesicle release in the presence of cholesterol as a sole
405 carbon source (**Fig 5B**), as measured by dot blot after normalization to colony forming
406 units (CFUs). These results strongly suggest that cell envelope permeability determines
407 the magnitude of the vesiculation phenomenon in *Mtb*.
408 We next investigated whether common transcriptional features underpin the
409 regulation of cell envelope permeability in the tested conditions. To do that, we compared
410 the transcriptional response of *virR*^{mut} with that of available datasets including *Mtb*
411 cultured in the presence of 0.01% of cholesterol as a sole carbon source (Pawełczyk et
412 al., 2021), and *Mtb* treated with 6 μg ml^{-1} of TRZ (Dutta et al., 2010). Experimentally, we
413 retrieved the set of genes up and down-regulated in *Mtb* grown in cholesterol vs glucose-
414 rich culture media (Brzostek et al., 2009), and interrogated whether those genes were
415 enriched among the sets of differentially expressed genes in *virR*^{mut} vs WT reported in
416 this study (**Fig 5C**). Interestingly, we found that those genes whose expression changed
417 in the same direction in conditions associated with low, or high permeability, in both
418 studies were mutually enriched, while the cross-comparisons between sets with opposite

419 responses to low-permeability-associated treatments in both studies led to significant
420 depletion statistics. These results validate the initial hypothesis according to which
421 changes in permeability induced by these two treatments are linked to the activation of
422 a common transcriptional program. The inspection of genes that are simultaneously
423 upregulated in treatments associated with low permeability in both studies identified
424 DosR as a putative regulator associated with the orchestration of this transcriptional
425 footprint of low cell permeability. The two-component system DosS-DosR has a well-
426 known role as a global regulator of the transition to dormancy, and its regulon is
427 consistently upregulated in non-permeable dormant bacteria (Honaker et al., 2009).
428 Interestingly, authors found that low-permeability bacteria cultured in a cholesterol
429 medium, albeit featuring a regular growing phenotype, activated the DosR regulon,
430 suggesting that cell wall remodeling leading to a decrease in permeability linked with the
431 induction of DosR can be triggered independently to the transcriptional regulatory
432 programs leading to growth arrest and dormancy in *Mtb* (Pawełczyk et al., 2021).
433 Importantly, the integration of the genes that are down-regulated in *virR*^{mut} validates this
434 hypothesis (**Fig 5D** and **FigS5**), since 39 out of the 48 genes annotated in the DosR
435 regulon are simultaneously up-regulated in conditions linked to low permeability in both
436 studies.
437 A similar analytic approach for the comparison of the response of *virR*^{mut} and the
438 response to the drug Thioridazine, a treatment well-known for inducing an increase in
439 permeability in *Mtb*-treated cells (Dutta et al., 2010) (GSE16626), led to conceptually
440 similar results, with both genes simultaneously upregulated in both TRZ and *virR*^{mut}
441 (OR=1.51, p=0.03), as well as genes simultaneously down-regulated (OR=1.48, p=0.03),
442 being marginally enriched. Interestingly, among the 20 genes showing the largest, and
443 most significant repression effects by both treatments (log2FC>0.5 & FDR<0.05 in both
444 analyses), we found 6 genes whose functions are related with metal nutrients uptake,
445 homeostasis and metabolism, such as genes encoding the bacterioferritin BrfB,
446 rubredoxins RubA and RubB, metal homeostasis sensors CsoR (copper) and kmtR
447 (nickel and cobalt), and the metal exporter CtpJ (**Fig 5E**). Taken together, these analyses
448 highlight the transcriptional parallels between *virR*^{mut} and both TRZ and cholesterol
449 conditions, which strongly suggests the existence of a common transcriptional signature
450 associated with the control of cell permeability.
451
452 **The absence of VirR leads to an aberrant enlargement of PG in *Mtb*.** To elucidate
453 the specific molecular defects that explain the periplasm enlargement, the enhanced
454 permeability, and the antibiotic sensitivity phenotypes, we performed a biochemical
455 analysis of WT and *virR*^{mut} cell envelopes. First, we analyzed the total lipid profile by

456 liquid chromatography-mass spectrometry (LC-MS) and observed significant differences
457 in prevalent polar lipids linked to the cell membrane including, lysophosphatidic and
458 phosphatidic acid, species of monoacylated and diacylated glycerol,
459 phosphatidylethanolamines and phosphatidyl-myo-inositol mannoside (PIM) species,
460 being more abundant in *virR*^{mut} relative to WT and complementing strain. (**Fig 6A**). To
461 validate these results, we ran thin layer chromatography (TLC) analysis on the same lipid
462 extracts and found that the mutant carries more phospholipids in the membrane including
463 more $AcPIM_2$ and PE (**Fig 6B**). Moreover, we could not measure major differences in the
464 level of mycolic acid species (**Fig 6C**), while significantly more PDIMs were detected in
465 the mutant relative to the other strains (**Fig 6D**). This later result agrees with that of
466 transcriptomics and proteomics analyses. When analyzing apolar lipids we also
467 observed increased levels of free mycolic acids (FMA) and free fatty acids (FFA) upon
468 *virR* deletion (**Fig 6E**). The enhanced release of these apolar lipids has also been
469 documented in a *C. glutamicum* mutant in Cg0847 (Baumgart et al., 2016), a canonical
470 LCP protein. Importantly, we could not detect any of these lipids in EVs from *virR*^{mut} (**Fig**
471 **6F**), while major polar phospholipids could be resolved in EVs from all strains (**Fig 6G**),
472 as previously reported (R Prados-Rosales et al., 2011). This result indicates that *Mtb*
473 releases free apolar lipids independently from membrane associated EVs.
474 Next, we performed a glycosyl composition analysis of isolated cell walls
475 (including mycolyl-arabinogalactan-peptidoglycan complex) and determined that there
476 were no significant differences between strains in AG content as well as in the ratio
477 between arabinose and galactose (A/G) (**Fig 7A**). Similarly, no changes were observed
478 in the galactan length as measured by the ratio between galactose (G) and rhamnose
479 (R) G/R) (Justen et al., 2020). We noticed that the ratio between N-acetylglucosamine
480 (NAGc) and rhamnose (R) (NAGc/R) was significantly higher in *virR*^{mut} relative to WT,
481 suggesting an increase in PG content in this strain (**Fig 7A**). The validation of these
482 results was performed independently by measuring the amount of diaminopimelic acid
483 (DAP) in isolated cell walls, as a surrogate of PG content, and determined that *virR*^{mut}
484 carries two times more PG than WT or complemented strains (**Fig 7B**). We next obtained
485 pure PG preparations of each strain and performed an analysis by atomic force
486 microscopy (AFM) (**Fig 7C and Fig S6**). This technique has been recently used to
487 investigate the nanometric features of isolated Gram-positive bacterial cell walls
488 (Pasquina-Lemonche et al., 2020). Semi-automated analysis of liquid AFM images from
489 mycobacterial isolated PG samples revealed that: (i) the absence of VirR leads to a
490 significant reduction in PG pore diameter (down to 9.2 ± 0.6 nm) relative to WT (16 ±
491 3.3 nm) and complemented strains (10 ± 0.8 nm) (**Fig 7C, D and Fig S6**); (ii) the number
492 of pores is significantly higher in *virR*^{mut} compared to WT and complemented strain (**Fig**

493 **7E and Fig S6**); (iii) manual analysis of AFM images in ambient conditions revealed that
494 *virR*^{mut} PG is significantly thicker than that of the other strains of the study (**Fig 7F**). These
495 results show for the first time the nanometric architecture of isolated PG in mycobacteria
496 by AFM and suggest a role for VirR in regulating PG thickness and porosity. Strikingly,
497 we found that the PG enlargement observed in the *virR*^{mut} correlated with increased
498 susceptibility to the muramidase lysozyme (**Fig S7**), indicating modifications in PG
499 remodeling in *virR*^{mut}. Collectively, although the structural changes at nanoscopic level
500 of the peripheral areas of the cell observed by AFM leads to a more dense and thick
501 structure harder to penetrate, the chemical changes in the peptidoglycan structure
502 observed and biochemical assays suggest that changes associated with alterations in
503 VirR-regulated PG remodeling makes the wall more permeable and support increased
504 release of EV in *Mtb*.
505
506 **VirR interacts with canonical LCP proteins**. As mentioned above VirR is a LytR_C
507 solo domain protein with no catalytic LCP domain. Other members of the LCP protein
508 family like Rv3267 and Rv3287 are the main PG-AG ligases (Grzegorzewicz et al., 2016;
509 Harrison et al., 2016) and also carry a LytR_C domain. We have previously shown that
510 VirR interacts with itself (Rath et al., 2013). Consequently, we reasoned that if VirR
511 contributed to PG-AG ligation it could do it via interaction with canonical LCP proteins
512 through the LytR_C domain. Although VirR is one of the most abundant proteins found
513 in tuberculin preparations (Prasad et al., 2013), we determined that it localizes at sites
514 of nascent cell wall by fluorescence microscopy (**Fig S8**). Therefore, its location could
515 initially allow for interactions with other cell surface proteins like LCP. Both recombinant
516 VirR and the main AG-PG ligase Lcp1 (Rv3267) oligomerize in a blue-native PAGE gel
517 (**Fig 8A**). This observation suggests that they interact with proteins sharing similar
518 domain features. We next performed a flotation assay where we examined the behavior
519 of VirR on an iodixanol gradient in the presence or absence of Lcp1. Using a specific
520 antibody raised against VirR, we observed that the presence of Lcp1 displaces the
521 relative location of VirR toward upper fractions of the gradient, indicating a potential
522 interaction of both proteins and the formation of higher molecular weight complexes (**Fig
523 8B**). To investigate the interaction of virR and Lcp1, along with other Lcp proteins, in a
524 more physiological environment we used the bipartite splitGFP approach (Cabantous et
525 al., 2013) (**Fig 8C and Fig S9**), which has been recently utilized to demonstrate the co-
526 localization and interaction of the membrane-bound metal ATPase CtpC with the
527 chaperon PacL1 (Boudehen et al., 2022). We first recapitulated the VirR self-interaction
528 and added that such interaction implicates the LytR_C domain since no differences in
529 fluorescence were measured between full and truncated versions of VirR (VirRsol)

530 lacking the first 41 amino acids. As negative controls, we included interactions between
531 VirR and the cell surface associated metal ATPase CtpC (**Fig 8D**). When testing
532 interactions between VirR and other Lcp proteins (Rv0822c, Lcp1 (Rv3267) and Rv3284)
533 we could not measure any GFP signal when full Lcp proteins were used in the assay.
534 Conversely, a significant increase in fluorescence was measured for all combinations
535 when truncated Lcp proteins including either the C-terminal domain or specifically the
536 LytR_C domain were tested (**Fig 8C**). These results strongly suggest that VirR interacts
537 with Lcp proteins and that these interactions occur via LytR_C terminal domains.
538
539 **DISCUSSION**
540 Our group reported *virR* as the first gene implicated in the biogenesis of EVs in *Mtb* ten
541 years back (Rath et al., 2013). A transposon mutant in *virR* (*virR*^{mut}) overproduces MEVs
542 and this provokes augmentation of cytokine responses in mouse and human
543 macrophages. This mutant manifested an attenuated phenotype in experimental
544 infections on macrophages and mice (Beaulieu et al., 2010; Rath et al., 2013). Such
545 studies established that VirR has a role in virulence by negatively modulating the release
546 of MEVs. These studies provided evidence that vesiculogenesis in *Mtb* is genetically
547 regulated. Since then, conditions such as iron starvation (Prados-Rosales et al., 2014b)
548 and other genes including *iniAC* (Gupta et al., 2023) and the Pst/SenX3-RegX3 signal
549 transduction system (White et al., 2018) have been shown to contribute to the biogenesis
550 of MEVs. Interestingly, VirR, a LytR_C solo domain protein (**Fig S1**), shares homology
551 with Lcp proteins, which in *Mtb* are known to participate in the enzymatic connection
552 between AG and PG (Grzegorzewicz et al., 2016; Harrison et al., 2016). This suggests
553 VirR function might be linked to cell wall remodeling.
554 In this study, we investigated how VirR can control the magnitude of MEV release
555 in *Mtb*. We did this by studying the underlying enhanced vesiculogenesis phenomenon
556 observed in *virR*^{mut} using genetic, transcriptiomics, proteomics and ultrastructural and
557 biochemical methods. It was clear from our cryo-EM studies that *virR*^{mut} has an aberrant
558 cell wall as the layer above the cell membrane was significantly larger than that of WT
559 and complemented strains. The enlarged compartment showed higher granular texture,
560 a feature that has been previously associated to PG precursors in unrelated Gram-
561 positive bacteria (Zuber et al., 2006). This observation and previous studies showing the
562 increased sensitivity of *VirR*^{mut} to vancomycin (Ballister et al., 2019) strongly suggested
563 that the cell wall defect is connected to PG remodeling. The use of AFM on isolated PG
564 confirmed this and showed for the first time the nanostructure of PG in *Mtb*, providing
565 information on PG thickness, pore size and number of pores. AFM indicated that *virR*^{mut}
566 PG is thicker, has significantly more pores of small size. Considering the pore sizes

567 measured across strains (ranging from 9-16 nm), we initially ruled out the notion that
568 EVs (which are spheres of 50-300 nm in diameter) are released through the peripheral
569 cell wall. Therefore, *Mtb* must have an alternative mechanism to release EVs, possible
570 during the division process where the PG is most fragile, presumably due to defects in
571 crosslinking. These events were not possible to visualize in AFM given that PG
572 fragments from all the strains were lacking the poles or clearly defined division sites but
573 could be the subject of further studies in the future.

574 A recent study showed that *Corynebacterium glutamicum* can produce and
575 release different types of MVs through different routes, including the mycomembrane
576 blebbing or bubbling cell death depending on the stress at which *C. glutamicum* is
577 exposed (Nagakubo et al., 2021). In the present study, we have shown that $virR^{mut}$
578 overproduces EVs under normal growth conditions in the absence of cell lysis, according
579 to our assay which measured cytoplasmic leaking of the transcription factor IdeR..
580 Overall, we show that EV production in Mtb under our growing conditions, is not linked
581 to cell death. This fact largely excludes the bubbling cell death mechanism. Moreover,
582 our lipidomic analysis now and before (Rafael Prados-Rosales et al., 2011) indicates the
583 absence of mycomembrane lipids in isolated MEVs from all strains. These analyses rule
584 out that MEVs originate at the mycomembrane. These apparent disagreements with the
585 *C. glutamicum* study (Nagakubo et al., 2021) might indicate that *Mtb* EV biogenesis may
586 differ from that of *C glutamicum*, and other mycolic acid-containing bacteria with shorter
587 fatty acids. Additional variables that may explain differences between studies is the
588 growth media and the time at which vesicles are isolated (Gupta et al., 2023). Of note,
589 *M. smegmatis* EVs were isolated at day 6 (Nagakubo et al., 2021), a time at which this
590 fast-growing mycobacteria is already in stationary phase.

591 The transcriptional profile of $virR^{mut}$ can provide a partial explanation for the
592 attenuated phenotype of the mutant due to a downregulation of genes activated upon
593 stresses associated to the intraphagosomal environment. It is particularly interesting to
594 observe the specific reduction in the transcript level of the two most important effectors
595 of the esx-1 secretion system. On the other hand, genes involved in PDIM synthesis
596 were upregulated. It is possible that the specific upregulation of PDIM synthesis in
597 absence of *virR* is part of compensatory response to a reduced permeability. We were
598 surprised to find no differences between protein profiles in whole cells between WT and
599 $virR^{mut}$ strains, despite difference in transcriptomics. A biological interpretation of these
600 results would point to the existence of global compensatory mechanisms of post-
601 transcriptional regulation used by the bacteria to partially recover comparable proteomic
602 profiles in $virR^{mut}$ to those observed in the WT.

603 Contrary to whole cell lysates, EV protein profiles between *virR*^{mut} and WT were
604 largely different. In this context, it is accepted that certain proteins and lipids are enriched
605 in bacterial EVs and that preferential inclusion of proteins and lipids in bacterial MVs
606 supports a specific vesicle biogenesis mechanism. In Gram positive bacteria and
607 mycobacteria both membrane and cytosolic proteins are included in EVs since the origin
608 of these structures is linked to the cell membrane (R Prados-Rosales et al., 2011) and,
609 presumably, the incorporation of intracellular proteins may occur during the process of
610 vesicle formation. We found a higher abundance of proteins related to PG and MA
611 synthesis in *virR*^{mut} EVs relative to WT. Therefore, these two processes seem to
612 contribute to EV biogenesis in *Mtb*. Additional data presented in this study, which
613 includes ultrastructural and chemical analyses confirm this. Both PG and MA synthesis
614 are complex processes, including a diverse set of genes. What parts of the biogenesis
615 of these molecules are important for the formation of EVs is a matter of future
616 investigations.
617 Another finding of the study is the connection between permeability and the
618 magnitude of the vesiculation process in *Mtb*. We linked these two phenomena first, by
619 measuring enhanced vesiculation and permeability in the same strain (*virR*^{mut}) and
620 second, by modifying the permeability using chemical (via sublethal exposure to TRZ)
621 and nutritional supplements (via providing cholesterol as sole carbon source) in WT *Mtb*.
622 TRZ, a repurposed drug that belongs to the class of phenothiazines, is known to affect
623 respiration in *Mtb* (Amaral et al., 1996). It is also assumed that TRZ can inhibit efflux
624 pumps leading to an increased susceptibility to first line antitubercular drugs when tested
625 in combination (De Knegt et al., 2014). This provides an explanation for the synergistic
626 effects of such combinations. An independent explanation of such synergy may also
627 come from the increased permeability, as it has been recently shown by a quantitative
628 proteomics analysis of *Mtb* cells exposed to sublethal concentration of TRZ (De Keijzer
629 et al., 2016). When we grew *Mtb* with cholesterol as a sole carbon source, a condition
630 that slows mycobacterial growth but also reduces cell permeability via cholesterol
631 accumulation in the cell wall (Brzostek et al., 2009), we observed the opposite trend on
632 MEV biogenesis. We consider this finding of high relevance since *Mtb* permeability is
633 one the major concerns when developing potential antimycobacterial drugs.
634 Nevertheless, bacterial cell permeability is a complex property that it is controlled by
635 physiochemical, biological, and chemical processes such as stereochemistry,
636 lipophilicity, saturation and unsaturation, flexibility, viscosity, fluidity, pressure,
637 temperature and physiological conditions (Nagamani and Sastry, 2021). How these
638 variables change to allow the release of MEVs is not known.

639 This study also proposes a model VirR function whereby VirR may work as a
640 scaffold for canonical Lcp proteins, which in *Mtb* links PG to AG. Based on the
641 demonstration that VirR interacts with canonical Lcp proteins, we believe that the
642 absence of VirR deregulates the localization of canonical Lcp proteins. Although we
643 cannot rule out the contribution of other phenomena including alteration of the PG
644 molecule, VirR is a central scaffold in the cell wall remodeling process. Taking into
645 consideration the fact that *VirR*^{mut} is attenuated in virulence on preclinical models of
646 infections and manifests an enhanced vesiculogenesis and permeability, VirR may
647 represent a novel and interesting drug target. We envision that targeting VirR may not
648 only make *Mtb* weaker and more permeable to other antitubercular drugs, but to
649 stimulate the immune system, via MEVs, to fight infection.
650
651 **MATERIALS AND METHODS**
652
653 **Bacterial Strains, media and growth conditions.** *Mtb* H37Rv (ATCC) and derivative
654 strains *virR*^{mut} and *virR*^{mut}*-C* (complemented strain) (Rath et al., 2013) were used in this
655 study. Bacteria were initially grown in Middlebrook 7H9 medium (7H9) supplemented
656 with 10% (v/v) OADC enrichment (Becton Dickinson Microbiology Systems, Spark, MD),
657 0.5% (v/v) glycerol and with Tyloxapol 0.05% (v/v; Sigma) prior to inoculation in a minimal
658 medium (MM) consisting of KH_2PO_4 1 g/l, Na_2HPO_4 2.5 g/l, asparagine 0.5 g/l, ferric
659 ammonium citrate 50 mg/l, $CaCl_2$ 0.5 mg/l, $ZnSO_4$ 0.1 mg/l, without Tyloxapol 0.05%
660 (v/v), containing 0.7% (v/v) glycerol, pH 7.0.
661 *Mtb* was also cultured in 7H9 medium in the presence of sublethal concentrations of
662 thirodazine (TRZ) of 6 ug ml as previously described. We determined that this
663 concentration does not affect cell growth. *Mtb* was also cultured in MM with cholesterol
664 as a sole carbon source as previously described (Brzostek et al., 2009).
665 *Mtb* expressing fluorescent VirR was generated by cloning VirR into pmv261-Venus
666 using fast cloning approach (Li et al., 2011).
667 *M. smegmatis* mc^{2}155 (ATCC 700084) and recombinants derived from this strain were
668 grown at 37°C in 7H9 medium (Difco) supplemented with 10% albumin-dextrose-
669 catalase (ADC, Difco) and 0.05% Tween-80 (Sigma-Aldrich), or on complete 7H11 solid
670 medium (Difco) supplemented with 10% oleic acid-albumin-dextrose-catalase (OADC,
671 Difco). When needed, streptomycin (25 μg.ml^{-1}) was added to the culture media.
672 *Escherichia coli* strains StellarTM (Takara bio) were grown at 37˚C in LBroth (Difco) or
673 on L-agar plates (Difco) supplemented with streptomycin (25 μg.ml^{-1}) when required.
674

675 ***M. smegmatis* expression vectors for split GFP experiment.** Plasmids used for split
676 GFP experiments were constructed by modifying the plasmid pGMCS-PpacL1-pacL1-
677 Lk2-GFP11-ctpC(1-85)-Lk15-GFP(1-10) (Boudehen et al., 2022) (**Table S1**). Plasmids
678 pGMCS, conferring resistance to streptomycin, are shuttle vectors, episomal in *E. coli*
679 and integrative in mycobacteria through insertion at the attL5 mycobacteriophage
680 insertion site in the glyV tRNA gene. Lk2 (LEGSGGGGSGGGS) and Lk15
681 (GPGLSGLGGGGGSLG) are flexible linkers separating the protein domains of interest
682 from the last 11th b-sheet or the first ten b-sheets of GFP, respectively. First, the Zinc-
683 inducible PpacL1 promoter was replaced by P1, a strong constitutive promoter from *M.*
684 *smegmatis* (Ariyachaokun et al., 2020), resulting in pGMCS-P1-pacL1-Lk2-GFP11-
685 ctpC(1-85)-Lk15-GFP(1-10). Second, the pacL1 (Rv3269) sequence was replaced by
686 that of virR (encoding amino-acids 1 to 164) or virRsol (encoding amino-acids 42 to 164)
687 by In-Fusion HD cloning (Takara). PCR fragments were amplified using appropriate
688 primer pairs (**Table S1**) and Phusion High-Fidelity PCR Master Mix with GC Buffer
689 (Thermo Scientific, Walthman, MA United States). Linear fragments were purified on
690 agarose gels and inserted into pGMCS backbone linearized by PCR amplification with
691 appropriate primers, using the In-Fusion HD Cloning Kit (Takara), following the
692 manufacturer's instructions. Finally, the ctpC sequence was replaced on the resulting
693 plasmids by the virR or virRsol sequences, or that encoding either the C-terminal part or
694 only the LytR_C domains of the Rv0822c, Rv3267 or Rv3484 proteins from M.
695 tuberculosis H37Rv. Plasmids were constructed by transformation into *E. coli* Stellar
696 recipient cells. All plasmids were verified by sequencing before introduction by
697 electroporation into *M. smegmatis* mc²155 strain.
698
699 **Generation of the CRISPR mutants.** To generate the conditional CRISPR mutants we
700 took advantage of the CRISPR interference (CRISPRi) technology (Rock et al., 2017).
701 Briefly, we designed sgRNA oligonucleotides containing the target Rv0431 (*virR*) and
702 Rv2700 (*cei*) genes sequences (Table S1) located immediately upstream of the PAM
703 sequence. The strengths of the PAM sequence were chosen following authors
704 recommendation to get high and intermediate gene repression, 158.1 or 42.2-fold
705 repression for *virR* and 145.2 and 47.3 for *cei*, respectively. The primers were annealed
706 and ligated into the gel purified BsmBI-digested CRISPRi vector (pIJR965 plasmid)
707 followed by transformation of competent *Mtb* cells via electroporation. Transcriptional
708 knockdown of genes were quantified by qRT-PCR; and protein levels were examined by
709 immunoblot using specific antibodies raised against VirR (Rath et al., 2013) and Cei
710 (Ballister et al., 2019) **.**
711

712 **EV isolation and purification.** *Mtb*-EV were prepared and purified as previously
713 described. Briefly, the culture filtrate of 1 L cultures of Mtb grown in low iron MM without
714 detergent for 14 days was processed for vesicle isolation by differential centrifugation. In
715 parallel a 2 ml culture in MM supplemented with 0.05% tyloxapol to disperse bacterial
716 clumps was used to determine viability by plating culture dilutions onto 7H10 agar plates
717 and enumerating colony forming unit (CFU) at the time of culture filtrate collection.
718 The membranous pellet containing vesicles obtained after ultracentrifugation of the
719 culture filtrate at 100,000 ×g for 2 h at 4°C, was resuspended in 1 ml sterile phosphate-
720 buffered saline (PBS) and overlaid with a series of Optiprep (Sigma-Aldrich) gradient
721 layers with concentrations ranging from 30% to 5% (w/v). The gradients were centrifuged
722 at 100,000 × g for 16 h. At the end 1 ml fractions were removed from the top, diluted to
723 20 ml with PBS and purified vesicles recovered by sedimentation at 100,000 × g for 1 h.
724 Vesicle pellets were suspended in PBS before analysis. Protein concentration was
725 measured by Bradford assay (Bio Rad, Hercules, CA United States) according to
726 manufacturer instructions. For all conditionis test from which EVs were isolated,
727 normalization was performed by referring EVs concentration to colony forming units
728 (CFUs).
729
730 **Nano particle tracking analysis (NTA).** NTA was conducted using ZetaView (Particle
731 Metrix, Winning am Ammersee, Germany). Instrument calibration was performed prior
732 to EV analysis using 102 nm polystyrene beads (Thermo Fisher Scientific, Walthman,
733 MA United States), according to manufacturer instructions. Measurements were
734 performed using a 405 nm 68 mW laser and CMOS camera by scanning 11 cell positions
735 and capturing 60 frames per position at 25 C with camera sensitivity 85, shutter speed
736 100, autofocus and automatic scattering intensity. Samples were diluted in pre-filtered
737 PBS to approximately 106-107 particles·ml-1 in Millipore DI water. Analysis was
738 performed using ZetaView Software version 8.05.12 SP1 with a minimum brightness of
739 30, maximum brightness of 255, minimum area of 5, maximum area of 1000, and s
740 minimum trace length 15. Triplicate videos of each sample were taken in light scatter
741 mode. Particle size and concentration were analyzed using the built-in EMV protocol and
742 plotted using Prism software, version 8.0.1 (GraphPad Inc., San Diego, CA, United
743 States).
744
745 **Electron-Microscopy.** Cells were fixed with 2% glutaraldehyde in 0.1 M cacodylate at
746 room temperature for 24 h, and then incubated overnight in 4% formaldehyde, 1%
747 glutaraldehyde, and 0.1% PBS. For scanning microscopy, samples were then
748 dehydrated through a graded series of ethanol solutions before critical-point drying using

749 liquid carbon dioxide in a Toumisis Samdri 795 device and sputter-coating with gold-
750 palladium in a Denton Vacuum Desk-2 device. Samples were examined in a Zeiss Supra
751 Field Emission Scanning Electron Microscope (Carl Zeiss Microscopy, LLC North
752 America), using an accelerating voltage of 5 KV.
753 For Cryo-EM, grids were prepared following standard procedures and observed at liquid
754 nitrogen temperatures in a JEM-2200FS/CR transmission electron microscope (JEOL
755 Europe, Croissy-sur-Seine, France) operated at 200 kV. An in-column omega energy
756 filter helped to record images with improved signal/noise ratio by zero-loss filtering. The
757 energy selecting slit width was set at 9 eV. Digital images were recorded on an
758 UltraScan4000 CCD camera under low-dose conditions at a magnification of 55,058
759 obtaining a final pixel size of 2.7 Å/pixel.
760 Density profiles were calculated along rectangular selections with the ImageJ software
761 (NIH, Bethesda, MD). The number of cells analyzed varied from n = 20 (WT), n = 15
762 (*virR*^{mut}) and n = 23 (*virR*^{mut}-C). The comparisons extracted from this data is statistically
763 relevant with t test with Welch's correction performed. For each cell three representative
764 measurements were obtained. Mean and standard error was then calculated for
765 measurements pooled for each strain.
766
767 **Western Dot blot.** Two µl of EV isolates and two-fold serial dilutions were spotted onto
768 a nitrocellulose membrane (Abcam) and process for dot blot using anti-EV polyclonal
769 murine serum (Prados-Rosales et al., 2014a) as primary antibody and goat anti-mouse-
770 HRP conjugated as secondary antibody and ECL prime Western Blotting Detection
771 chemiluminescent substrate (GE Healthcare). The signal was visualized in a Chemidoc
772 MP imaging system (Bio Rad, Hercules, CA United States).
773
774 **RNA sequencing.** *Mtb* strains were grown in MM supplemented with 0.05% Tyloxapol
775 at 37ºC until they reached an OD595nm of 0.3 and harvested by centrifugation. The cell
776 pellets were resuspended in 1 ml Qiagen RNA protect reagent (Qiagen) and incubated
777 for 24 h at room temperature. Cells were disrupted by mechanical lysis in a FastPrep-
778 24 instrument (MP Biomedicals, Santa Ana, CA) in Lysing Matrix B tubes and RNA was
779 purified with the Direct-zol RNA miniprep kit (Zymo Research, Irvine, CA). The quantity
780 and quality of the RNAs were evaluated using Qubit RNA HS Assay Kit (Thermo Fisher
781 Scientific) and Agilent RNA 6000 Nano Chips (Agilent Technologies), respectively.
782 Sequencing libraries were prepared using the Ribo-Zero rRNA Removal Kit (Gram-
783 positive Bacteria) (Illumina Inc.) and the TruSeqStranded mRNA library prep kit (Illumina
784 Inc), following the Ribo-Zero rRNA Removal kit Reference guide and the
785 "TruSeqStranded mRNA Sample Preparation Guide. Briefly, starting from 1 µg of total

786 RNA, bacterial rRNA was removed and the remaining RNA was cleaned up using
787 AgencourtRNAClean XP beads (Beckman Coulter). Purified RNA was fragmented and
788 primed for cDNA synthesis. cDNA first strand was synthesized with SuperScript-II
789 Reverse Transcriptase (Thermo Fisher Scientific) for 10 min at 25˚C, 15 min at 42˚C, 15
790 min at 70˚C and pause at 4˚C. cDNA second strand was synthesized with Illumina
791 reagents at 16˚C for 1 hr. Then, A-tailing and adaptor ligation were performed. Libraries
792 enrichment was achieved by PCR (30 sec at 98˚C; 15 cycles of 10 sec at 98˚C, 30 sec
793 at 60˚C, 30 sec at 72˚C; 5 min at 72ºC and pause at 4˚C). Afterwards, libraries were
794 visualized on an Agilent 2100 Bioanalyzer using Agilent High Sensitivity DNA kit (Agilent
795 Technologies) and quantified using Qubit dsDNA HS DNA Kit (Thermo Fisher Scientific).
796 Library sequencing was carried out on an Illumina HiSeq2500 sequencer with 50
797 nucleotides single end reads and at least 20 million reads per individual library were
798 obtained.
799
800 **RNA-sequencing data analysis.** Quality Control of sequenced samples was performed
801 by FASTQC software (http://www.bioinformatics.babraham.ac.uk/projects/fastqc/).
802 Reads were mapped against the *M. tuberculosis* H37Rv strain
803 (GCF_000195955.2_ASM19595v2) reference genome using Tophat (Trapnell et al.,
804 2009) with --bowtie1 option, to align 50 bp reads. The resulting BAM alignment files for
805 the samples were the input to Rsubread's (Liao et al., 2019) featureCounts function to
806 generate a table of raw counts required for the Differential Expression (DE) analysis.
807 Data preprocessing and differential expression analysis of the transcriptomic data was
808 performed using DeSeq2 (Love et al., 2014). Genes with a median of expression lower
809 than 1 CPM, and genes containing outlier observations were filtered before statistical
810 modeling, and the remaining N=4004 genes were used for differential expression
811 analysis. P-values were corrected for multiple testing using the R package, implementing
812 the Storey-Tibshirani FDR correction method (Storey et al., 2023). Genes with an
813 FDR<0.05 were deemed as differentially expressed. Data were deposited at Gene
814 expression Omnibus (GEO); GSE143996.
815
816 **Label-free mass spectrometry analysis**. Total cell proteins and MEV-associated
817 proteins were submitted to LC-MS label-free analysis using a Synapt G2Si ESI Q-
818 Mobility-TOF spectrometer (Waters) coupled online to a NanoAcquity nano-HPLC
819 (Waters), equipped with a Waters BEH C18 nano-column (200mm x 75 um ID, 1.8um).
820 Samples were incubated and digested following the filter-aided sample preparation
821 (FASP) protocol (Wiśniewski et al., 2009) Trypsin was added to a trypsin:protein ratio of
822 1:50, and the mixture was incubated overnight at 37°C, dried out in a RVC2 25 speedvac

823 concentrator (Christ), and resuspended in 0.1% FA. Peptides were desalted and
824 resuspended in 0.1% FA using C18 stage tips (Millipore). Digested samples (500 ng)
825 were loaded onto the LC system and resolved using a 60 min gradient (5 to 60% ACN).
826 Data was acquired in HDDA mode that enhances signal intensities using the ion mobility
827 separation step. Protein identification and quantification were carried out using
828 Progenesis LC-MS (version 2.0.5556.29015, Nonlinear Dynamics). One of the runs was
829 used as the reference to which the precursor masses in all other samples were aligned
830 to. Only features comprising charges of 2+ and 3+ were selected. The raw abundances
831 of each feature were automatically normalized and logarithmized against the reference
832 run. Samples were grouped in accordance to the comparison being performed, and an
833 ANOVA analysis was performed. A peak list containing the information of all the features
834 was generated and exported to the Mascot search engine (Matrix Science Ltd.). This file
835 was searched against a Uniprot/Swissprot database, and the list of identified peptides
836 was imported back to Progenesis LC-MS. Protein quantitation was performed based on
837 the three most intense non-conflicting peptides (peptides occurring in only one protein),
838 except for proteins with only two non-conflicting peptides.
839
840 **Proteomics data analysis**. Normalization and imputation of the proteomics data was
841 done using the DEP package for R (Zhang et al., 2018). Normalization was done using
842 the vsn method (Huber et al., 2002), which transforms data tackling heteroskedasticity.
843 Imputation of missing values was performed using the bpca method (Oba et al., 2003),
844 which leans on principal component analysis to impute missing values.
845 Data was analyzed according to a design where differences between strains (*virR*^{mut}-
846 WT) were estimated independently within each cell compartment, (whole cell lysates or
847 EVs). according to a nested design: Expression ~ Compartment + Strain:Compartment.
848 Differential expression analysis of the proteomics data was performed using limma
849 (Ritchie et al., 2015) and p-values were corrected for multiple testing according to the
850 Storey-Tibshirani method using the R package qvalue (Storey et al., 2003). Proteins with
851 an FDR<0.05 were selected as differentially expressed.
852
853 **Gene ontology (GO) enrichments.** Enrichment analyses of the sets of differentially
854 expressed genes and proteins were performed in R using the terms of the Gene
855 Ontology database for testing, version 11.02.2020. Gene sets corresponding to the
856 biological process and cellular component ontologies within levels 4 to 6 (N=2245) were
857 selected and filtered according to their size (minimum size =10 in the RNAseq analyses;
858 and =3 in the proteomics analyses). The selected sets were tested for enrichment using
859 Fisher's exact test. Multiple testing correction was performed using the qvalue R package

860 (Storey et al., 2023). Terms with a FDR < 0.1 and an odds ratio > 2 were selected for
861 visualization in figures 3D, and 4D, where node sizes was proportional to the significance
862 of the enrichments. In these visualizations, two terms were connected depending on the
863 amount of sharing between the groups of genes contributing to the enrichments in each
864 of them, drawing a link whenever the intersection between the groups of genes was
865 larger than 50% of the smallest of the two gene sets involved. Ontology term clusters,
866 represented by colors, were then assigned using the Louvain's algorithm for modularity
867 optimization (Blondel et al., 2008), as implemented in the R package igraph (Csardi and
868 Nepusz, 2006). Visualization of the resulting networks was done using the open-source
869 software Gephi (Bastian et al., 2009).
870
871 **Targeted metabolomics.** LC-MS analysis was carried out on a Schimazdu LC/MS-8030
872 coupled with a triple quadrupole mass analyser (QqQ) provided with an electrospray
873 source in a negative ionization mode. Extracted metabolites were quantified in Multiple
874 Reaction Monitoring (MRM) mode. A stock standard solution prepared in 17% (v/v)
875 methanol in water and containing all metabolites: acetyl-CoA, methyl citrate,
876 methylmalonyl-CoA, pyruvate, was used as external standard. Metabolites were
877 identified by ion pairing liquid chromatography. Acetyl-CoA, methyl citrate and
878 methylmalonyl-CoA were separated by reverse phase with a poroshell 120 Phenyl-Hexyl
879 analytical column (2.1 x 50mm, 2.7 µm, Agilent) and a binary gradient (**Table S2**)
880 consisting of a mobile phase A with water-methanol 97:3 (v/v), 10 mM tributylamine and
881 3 mM acetic acid, and mobile phase B composed of pure methanol. Pyruvate was
882 separated by normal phase using a Kinetex HILIC analytical column (2.1 x 150 mm, 2.6
883 µm, Phenomenex) and a binary gradient (**Table S3**) consisting of pure water as mobile
884 phase A and pure methanol as mobile phase B.
885 The flow rate was maintained at 0.4 mL/min and the injection volume was 20 µL. Nitrogen
886 was used as nebulizing and drying gas at a flow rate of 1.5 and 15 mL/min, respectively.
887 The desolvation line (DL) temperature was set at 250 °C and the ionization voltage was
888 fixed at 4.5 kV. Argon was used as collision gas to perform collision-induced dissociation
889 at a pressure of 230 kPa. The dwell time was set at 100 ms and the detection was
890 performed in MRM mode (detector voltage of 1.8 Kv), monitoring three transitions for
891 each compound. The transition with higher intensity was selected as quantitative
892 purposes (**Table S4**), while the other two were used for confirmation of the identity.
893
894 **Lipidomic analysis by UPLC-MS**. The effect of virR on relative abundance of different
895 cell wall lipids was characterized as had been done previously for MEVs (Prados-
896 Rosales et al., 2014b). Briefly, cell wall lipids were extracted from triplicate 10mL cultures

897 of wild type, *virR*^{mut}, and *virR*^{mut} complemented (*virR*^{mut}-C) strains overnight into 3mL 2:1
898 chloroform:methanol at room temperature, extracts were dried under nitrogen before
899 being dissolved in 0.75mL LC-MS grade 2:1:1 isopropanol:acetonitrile:water. Extracts
900 were separated on a Waters ACQUITY BEH C18 column UPLC heated to 55ºC and
901 eluted at a flow rate of 0.4mL/minute with 60:40 acetonitrile:water as mobile phase A and
902 90:10 isopropanol:acetonitrile as mobile phase B, both containing 10mM ammonium
903 formate and 0.1% formic acid. Initial condition was 40%, B which increased to 43% at 2
904 minutes, 50% at 2.1 minutes, 54% at 12 minutes, 70% at 12.1 minutes, 90% at 18
905 minutes before returning to initial condition at 18.1 minutes to complete the run at 20
906 minutes. The coupled Waters Synapt G2 q-TOF MS was operated in positive ion
907 resolution mode with the following conditions: capillary voltage 2kV, cone voltage 30V,
908 desolvation gas temperature 550□C, gas flow 900L/hour, source temperature 120ºC.
909 Mass spectra were acquired in centroid mode from 100-3000 m/z with scan times of 0.5
910 second. Leucine enkephaline was used as reference. Relative abundances of Mass-
911 retention time pairs were normalized to total ion current and lipid species were identified
912 using Mycomass (Layre et al., 2011) and Mtb LipidDB databases (Sartain et al., 2011).
913
914 **Lipidomic analysis by thin layer chromatography (TLC)**. Lipidomic analysis of both
915 whole cells and EVs by TLC was performed as previously described (Boldrin et al.,
916 2021). *Mtb* strains were grown at 37°C in standing Middlebrook 7H9 and when they
917 reached an OD595 of 0.2, cells were washed and transferred to MM. Cells were grown
918 until they reached an OD595 of 0.5. Further, cells were harvested by centrifugation at
919 3,500 rpm for 5 min, and pellets were heat-inactivated at 100°C for 1 h and used for lipid
920 extraction. Five milliliters 2:1 (vol/vol) chloroform-methanol was added to the cell pellet
921 and incubated at room temperature (RT) for 12 h with constant stirring. The organic
922 extract was separated by centrifugation (1,000 × g, 5 min, RT) and decantation. The
923 obtained pellet was extracted with 5 ml 2:1 (vol/vol) chloroform-methanol for 1 h at RT
924 with constant stirring and separated under the same conditions. The combined two
925 organic extracts (total lipids) were dried under a stream of nitrogen gas at RT and saved
926 for lipid analysis.
927 Polar lipids were separated by 2D-TLC by spotting 200 μg of total lipids on 60 F254 silica
928 gel plates (Merck) using chloroform, methanol, water (50:30:6) as a mobile phase 1 (first
929 dimension), and chloroform, acetic acid, methanol, and water (40:25:3:6) as mobile
930 phase 2 (second dimension). Analysis of PDIMs and TAGs was performed in a 1D-TLC
931 format. Two hundred μg of total lipids were spotted on the silica plates and separated
932 using 9:1 petroleum ether-diethyl ether as mobile phase. Free mycolates were separated
933 by 1D-TLC using chloroform/methanol/ammonium hydroxide (80:20:2) as mobile phase.

934 Mycolic acids were extracted and separated from cells as previously described (Vilchèze
935 and Jacobs, 2007). EV-associated lipids were separated and visualized following the
936 same procedures as for WCLs. Development of TLC plates was performed by repeating
937 the process of pulverizing the staining solution and heating the plate at 100°C 4 times.
938 The staining solution contained 10.5 ml 15% ethanolic solution of 1-naphthol, 6.5 ml 97%
939 sulfuric acid, 40.5 ml ethanol, and 4 ml water.
940
941 **PG isolation.** To obtain mycobacterial cell walls, whole cell pellets were resuspended in
942 PBS and boiled for 15 min. Boiled cells were transferred to 2 ml Lysing matrix tubes with
943 0.1 mm silica beads (M.P. Biomedical). And mechanically disrupted in a FastPrep-24TM
944 (M.P. Biomedical) giving 12 cylcles at predetermined speed of 6 during 30 s. Samples
945 were allowed to chill on ice for 3 min between cycles. Cell breakage was monitored by
946 optical microscopy (using Methylene blue as stain), if 95% of the cells had not broken
947 perform additional FastPrep-24TM cycles were performed. Lysed cells were centrifuged
948 at 170 x g for 30 s to separate them from beads and the supernatant were transferred to
949 a clean 1.5 ml tube. The suspensions were further digested with 10 µg of DNase and
950 RNase/ml for 1 h at 4°C to obtain a cell wall-enriched fraction after centrifugation at
951 27,000 × g for 10 min. Cell walls were resuspended in PBS containing 2% sodium
952 dodecyl sulfate (SDS) and the suspension was incubated for 1 h at 90°C with constant
953 stirring and recentrifuged at 27,000 × g for 30 min, and the supernatant was discarded.
954 This process was repeated twice. The resulting pellet was washed trice in distilled water,
955 80% acetone and acetone and lyophilized. Pellets were resuspended in 0.9 ml Tris-HCL
956 (50 mM, pH 7) buffer, plus 0.1 ml of protease K stock solution. The mixture was incubated
957 at 60 °C for 90 minutes, to digest any remaining surface proteins attached to the CW and
958 centrifuged again for 3 min at 20,000 g and resuspend pellet in distilled water. The
959 mixture was then heated at 90°C for 1 h before centrifugation at 27,000 × g for 30 min.
960 The supernatant was discarded and washed twice with PBS and four times with
961 deionized water to remove SDS. Pure PG was obtained from isolated cell walls. Briefly,
962 pure cell walls were resuspended in 0.5% KOH in methanol and stirred at 37°C for 4
963 days to hydrolyze mycolic acids (MA). The mixture was centrifuged (27,000 x g 20 min)
964 and the pellet was washed twice with methanol. MA were separated from cell walls using
965 diethyl ether and recentrifuged at 27,000 x g for 20 min. The supernatant contained
966 MAMEs. The extraction process with diethyl ether was repeated twice and let dry. The
967 resulting arabinogalactan (AG)-PG was digested with 0.2 N H2SO4 at 85°C for 30 min
968 and neutralized with $BaCO_3$ to remove the arabinogalactan. Treated AG-PG was
969 centrifuged at 27,000 g for 20 min. Supernatant contained soluble AG. The resulting

970 insoluble PG was washed four times by centrifugation in deionized water and stored at
971 4 ºC or room temperature.
972
973 **Analysis of diaminopimelic acid.** For DAP quantification (Tsuruoka et al., 1985),
974 samples were hydrolyzed overnight in 6N HCl at 100°C in 1ml capacity-crystal ampoules
975 (Wheaton). Samples were dried and resuspended in water and mixed in a 1:1:1 ratio
976 with pure acetic acid and ninhydrin reagent (250 mg ninhydrin, 4 mL phosphoric acid 0.6
977 M, and 6 mL pure acetic acid). Samples were measured at OD434 nm and the amounts
978 of DAP were calculated based on a standard curve with pure DAP. The data displays
979 the average ± standard deviations n=3.
980
981 **Glycosyl composition of isolated cell walls**. 500 µg of purified cell walls were mixed
982 with 10 µg of inositol and hydrolyzed with 0.1 M trifluoroacetic acid (TFA) for 2 h at 121
983 °C. The monosaccharides released were then converted into alditol acetates by
984 reduction with $NaBH_4$ and acetylation with acetic anhydride in pyridine. The products
985 were analyzed by gas chromatography-mass spectrometry in a 7890A/5975C system
986 from Agilent, using a DB-5ht (30 m x 0.25 mm x 0.1 µm) fused silica capillary column.
987 The compounds were identified by comparing the retention times of the peaks with those
988 recorded for standards analyzed under identical conditions. Quantification was carried
989 out considering the area of the peaks and the response factors of each compound with
990 respect to inositol.
991
992 **Atomic force microscopy and data analysis**. The dry pellets of purified peptidoglycan
993 from the three strains were dissolved in pure water and further broken by tip sonication
994 at 2 mA for 30 seconds, three cycles. Then 10 µL of the PG suspension was added to
995 standard AFM substrate made of mica coated with 0.01 % Poly-L-lysine by incubating
996 the sample during 90 min to achieve good coverage. The sample was further rinsed with
997 water and dried with Nitrogen flow. The AFM in ambient conditions (i.e. air) was
998 performed using Tapping mode in a Bruker FastScan Bio machine (Santa Barbara, US)
999 with Nunano SCOUT 350 - Silicon AFM probes (spring constant: 42 N/m, Resonance
1000 frequency: 350 kHz). The images were taken using a free amplitude of 10 nm with set
1001 point of 70-80 % of free amplitude (e.g. 7 nm). For AFM high resolution imaging in liquid
1002 the images were acquired in Peak force Tapping mode in imaging buffer made of 10 mM
1003 Tris and 150 mM KCl, pH: 8, with the FastScan Bio machine using Bruker Fastscan-D
1004 AFM probes (spring constant: 0.1 N/m, Resonance frequency: 70 kHz) at the force range
1005 of 1-3 nN peak force set point. The imaging parameters used are as follows; Scan rate:

1006 1 Hz; Scan angle: 0 °; Peak force amplitude: 80-100 nm and with high pixel resolution
1007 (512-880).
1008 The thickness measurements were performed with standard Gwyddion 1D height
1009 distribution tool (selecting an area containing background and a single leaflet of
1010 peptidoglycan). The number of cells analysed varied from n = 23 (for Mtb WT), n = 36
1011 (for *virR*^{mut}) and n = 25 (for *virR*^{mut}-C). The comparisons extracted from this data is
1012 statistically relevant with t test with Welch's correction performed. The analysis of the
1013 high-resolution images obtained in liquid was performed using the semi-automated
1014 custom-made routine from (Pasquina-Lemonche, et al. "Pore AFM", 2024) where the
1015 pore area, later converted in diameter, and the pore number were measured from the 2D
1016 slice of each image containing the maximum number of pores (see Fig. S8). The number
1017 of images similar to images shown in Fig. 5 were n = 8 for all strains, analyzing both pore
1018 size and pore number, the statistical comparisons were also performed using a t test with
1019 Welch's correction.
1020
1021 **Blue native PAGE.** Oligomerization of VirR and Lcp1 was analyzed by Blue native
1022 PAGE (Invitrogen). Recombinant VirR and Lcp1 proteins were prepared in 1xLB Native
1023 PAGE including DDM at 0.5% final concentration. After incubation at 4ºC for 30 min,
1024 samples were centrifuged at 20,000 x g for 30 min at 4ºC. The supernatant was
1025 recovered and mixed with G-250 additive following manufacturer instructions (Invitrogen)
1026 and loaded onto a Novex® Bist-Tris 4-16% gradient gel and run following manufacturer
1027 instructions. Gel was first fixed and then stained with Commassie.
1028
1029 **Liposome flotation assay**. Individual or combined VirR and Lcp1 were prepared at 2
1030 μM in buffer A in a final volume of 50 μl and incubated for 30 min at 37˚C. This volume
1031 was mixed with 100 µl of 60% optiprep (Sigma-Aldrich) to a final concentration of 40%
1032 and overlaid with 100 µl of subsequent optiprep solutions at 35%, 30%, 20% and 10%
1033 (optiprep solutions were prepared in Buffer A). The samples were centrifugated at 70000
1034 rpm for 2 h at 4°C in an Optima TLX Ultracentrifuge (Beckman Coulter, Indianapolis, IN
1035 United States). Eleven fractions of 50 µl were recovered and examined by dot blot
1036 (performed as previously described). Polyclonal antibodies raised against VirR and Lcp1
1037 were used as primary antibodies. Quantification of dotblots was performed in ImageJ as
1038 previously described (Schirmer et al., 2022). Briefly, integrated densities were calculated
1039 after background subtraction, and referred to wild type values to obtain the relative
1040 integrated intensities.
1041

1042 **Lysozyme and PG and AG susceptibility assays.** *Mtb* WT and *virR*^{mut} strains were
1043 grown in 7H9 media supplemented with ADC and tween 80 to an OD 540 of 0.2 and then
1044 diluted to an OD 540 of 0.1 with 7H9 containing 0 or 50 µg.ml-1 lysozyme (Sigma). The
1045 cultures were incubated with agitation at 37˚C and O.D 540 was monitored daily.
1046
1047 **Fluorescence microscopy**. The *Mtb* strain bearing the plasmid VirR-pMV261-Venus
1048 was grown in MM to an OD595nm of 0.4. At this stage, cells were harvested, washed
1049 three times in 1 × PBS (pH 7.4), resuspended in 1/3 – 1/6 volume of 4%
1050 paraformaldehyde (PFA) and incubated for 2 h at 37°C. Finally, the cells were washed
1051 twice in 1 × PBS and resuspended in 100–200 µl of PBS. Microscope slides were
1052 covered with 5 µl poly-L-lysine (Sigma) and excess poly-L-lysine was removed away with
1053 distillated water. A 20 – 40 µl aliquot was applied to pre-treated slides, allowed to air dry
1054 and covered with antifade solution (Prolong Gold, Invitrogen) and visualized under the
1055 fluorescence microscope using a 100x oil immersion objective on an Orca 12-ERG digital
1056 CCD camera (Hamamatsu Photonics) mounted on a Nikon E600 microscope.
1057
1058 **FACS analysis for split-GFP experiments.** *M. smegmatis* mc²155 transformed with the
1059 pGMCS derivatives were inoculated in complete 7H9 medium. After overnight incubation
1060 at 37°C, bacteria were collected and analyzed by fluorescence activated cell sorting
1061 using a BD FACS LSRFortessa X20 flow cytometer. Flow cytometry data analysis was
1062 performed using FlowJo software (Version 10; Becton, Dickinson and Company,
1063 Ashland, OR, USA). The gating strategy is displayed in supplementary figure 10 (Fig.
1064 S10).
1065
1066 **Statistical analysis.** The statistical significance of the difference between experimental
1067 groups was determined by the two-tailed Student's test using PRISM 5.0. P values ≤
1068 than 0.05 were considered significant. Statistical analysis of RNAseq is detailed in the
1069 corresponding section of Materials and Methods.
1070
1071 **Data Availability.** The Datasets produced in this study are available in the following
1072 database: RNA-seq data: Gene expression Omnibus, GSE143996
1073 (https://www.ncbi.nlm.nih.gov/geo/query/acc.cgi?acc=GSE143996).
1074
1075 **Funding Information.** R.P.-R. acknowledges support by MINECO/FEDER EU contracts
1076 SAF2016–77433-R, PID2019-110240RB-I00, PID2022-136611OB-I00; and NIH-
1077 R01AI162821. CICbioGUNE thanks MINECO for the Severo Ochoa Excellence
1078 Accreditation (SEV-2016–0644). L.P-L and J.K.H acknowledges support by the

1079 Wellcome Trust (212197/Z/19/Z) which funded part of this research. For the purpose of
1080 open access, the authors have applied and will apply a CC BY public copyright license
1081 to any Author Accepted Manuscript version arising from this submission. J.S.
1082 acknowledges support from the Spanish Ministry of Science and Innovation (MICINN)
1083 through grant PID2019-106859GA-I00 and Ramón y Cajal research grant RYC-2017-
1084 23560, as well as to the Government of Aragón, Spain, through grant B49-23R
1085 (NeuroBioSys). FC lab research is supported by the Swedish Research Council
1086 (VR2018-02823 and VR2018-05882), the Laboratory for Molecular Infection Medicine
1087 Sweden (MIMS), Umeå University, the Knut and Alice Wallenberg Foundation (KAW)
1088 grant KAW2012.0184 and the Kempe Foundation.
1089
1090 **Acknowledgments.** We are very grateful to Carl Nathan for sharing mutant *Mtb* strains.
1091 We thank G. Marcela Rodriguez for sharing the a-IdeR antibody. We thank Heran Darwin
1092 for sharing a-cei polyclonal antibody. We thank Emmanuelle Näser (Génotoul TRI-IPBS
1093 platform, Toulouse) for helping with flow cytometry. We thank Dr. Luke Alderwick
1094 (University of Birmingham) for the donation of the plasmid to recombinantly express Lcp1
1095 protein. We thank M. Gutiérrez for assistance with figures. The authors have no conflict
1096 of interest to declare.
1097
1098
1099
1100 **Figure Legends**
1101
1102 **Figure 1. Ultrastructural changes in the cell envelope of *virR*-deficient mutant**
1103 **associated with increased vesiculation.** (**A**) Cryo-electron micrographs of indicated
1104 *Mtb* strains grown in high iron MM. Closed line rectangles were used to calculate grey
1105 value profiles of cell envelopes using ImageJ. The dashed line insets within the main
1106 micrograph were magnified to show a detailed view of the cell surface. Scale bars are
1107 100 nm in main micrographs and 50 nm in the insets. (**B**) Density profiles based on grey
1108 values of the cross sections marked by solid line rectangles in A. (**C**) Mean values and
1109 standard errors of distances in nm between main cell envelope layers measured in A
1110 and C. *P < 0.05. CM, cytoplasmic membrane; OM, outer membrane; L1, layer 1; L2,
1111 layer 2. The number of cells analyzed varied from n = 20 (WT), n = 15 ($virR^{mut}$) and n =
1112 23 ($virR^{mut}$-C).
1113
1114 **Figure 2. Enhanced permeability and vesiculation are linked in the absence of**
1115 **LytR_C solo domain proteins in *Mtb*. (A)** Uptake of ethidium bromide (EthBr) in the

1116 indicated strains, as measured by fluorescence at 590 nm for 65 min. Data are mean and
1117 standard deviation of three biological replicates. **(B)** Sensitivity of the indicated strains to
1118 different concentrations of vancomycin as measured by monitoring optical density at 580
1119 nm (OD580) after 7 days. Data are mean and standard deviations of three biological
1120 replicated. Errors bars not shown are smaller than symbols. **(C)** Time course of the
1121 incorporation of FDAAs on the indicated strains in both 7H9 and MM as measured by
1122 fluorescence. Representative images of both WT and virR*mut* strains in either 7H9 or
1123 MM at 8h after the addition of the FDAA. Data are mean and standard deviations of three
1124 biological replicates. The arrow indicates the time at which images were taken. Errors
1125 bar not shown are smaller than symbols. **(D)** immunoblot analysis of cell lysates of two
1126 independent conditional mutants (c1 and c2) for virR and cei for the presence of VirR
1127 and cei proteins in cultures incubated with and without anhydrotetracycline (ATc). **(E)**
1128 Nanoparticle tracking analysis (NTA) of EV preparations derived from *virR* and *cei*
1129 conditional mutants (c2 (*virR*) and c1 (*cei*)) obtained from cultures with and without ATc
1130 showing number of particles per cm^3 determined by Zeta View NTA in three independent
1131 EV preparations. Data are presented as mean ± SEM.
1132
1133 **Figure 3. Transcriptional profiling of *virR^{mut}* showcases systemic alterations in cell**
1134 **wall architecture and metabolism. (A)** Experiment design for RNA-seq analyses. RNA
1135 was extracted from whole cell extracts from 4 replicate cultures of each strain (WT and
1136 *virR^{mut}*), and sequenced. Of these 8 samples, 7 passed quality control, (3 WT and 4
1137 *virR^{mut}*) and were subsequently analyzed. **(B)** PCA plot of the transcriptomics data. The
1138 loadings from the two first principal components are plotted. PC1 (X axis) significantly
1139 separates samples across strains (One tailed Mann Whitney test: PC1 in WT vs *virR^{mut}*:
1140 p=2.86 e-02). **(C)** Number of differentially expressed genes between *virR^{mut}* and WT.
1141 *virR^{mut}* significantly affects expression of a total of 750+913=1663 genes, (Storey-
1142 Tibshirani FDR=5%), which represents 41.5% of all genes tested. **(D)** Gene Ontology
1143 (GO) enrichments of downregulated genes in *virR^{mut}* (left) and upregulated ones (right).
1144 GO terms selected for testing included biological process and cell compartment labels
1145 containing $N \geq 10$ genes, between levels 4-6 of the ontology tree. In this representation,
1146 each node in the networks represents a significantly enriched term (terms selected for
1147 visualization with FDR=10% and enrichment odds-ratio>2), nodes' size is proportional to
1148 the enrichment significance, and links between terms are added wherever the sets of
1149 genes contributing to the enrichments in a connected pair show an intersection larger
1150 than 50% of the smallest of the gene sets involved in the pair (see Methods for further
1151 details, and supplementary table S2 for an extended list of all the enrichments found).
1152

1153 **Figure 4. *virR* regulates the protein content of EVs in *Mtb*. (A)**. Experiment design
1154 for proteomics analyses. label-free mass spectrometry data was retrieved for three
1155 replicates of H37RV and *virR*^{mut}. For each strain, in turn, data corresponding to proteins
1156 extracted from either whole-cell extracts (WC) and extracellular vesicles (EV) was
1157 produced, totaling 12 samples (2 strains times 2 cell compartments times 3 replicates).
1158 **(B)** PCA plot of the proteomics data. The loadings from the two first principal components
1159 are plotted. PC1 (X axis) significantly separates samples across cell-compartments
1160 (One-tailed Mann Withney test: PC1 in EV vs WC: p= 1.08 e-03), while PC2 separates
1161 samples from EVs in *virR*^{mut} from the rest of samples (one-tailed Mann Withney test: PC2
1162 in *virR*^{mut} in EV vs all other samples: p=4.55 e-03), indicating a differential peptidic cargo
1163 in the vesicles of *virR*^{mut}. **(C)** Bar plots of differentially expressed proteins found between
1164 strains in in whole cell extracts (left, 19 differentially expressed proteins at 5% FDR), and
1165 extracellular vesicles (right, 353 differentially expressed proteins at 5% FDR). **(D)** Gene
1166 Ontology enrichments of the downregulated proteins in the VirR mutant strain (left) and
1167 the upregulated ones (Right), at the EV location. GO terms selected for testing included
1168 biological process and cell compartment labels containing $N \geq 3$ genes, between levels
1169 4-6 of the ontology tree. As in figure 3D, terms selected for visualization with FDR=10%
1170 and enrichment odds-ratio>2, nodes' size is proportional to the enrichment significance,
1171 and links between terms are added wherever the sets of proteins contributing to the
1172 enrichments in a connected pair shows an intersection larger than 50% of the smallest
1173 of the gene sets involved in the pair (see Methods for further details, and supplementary
1174 table S2 for an extended list of all the enrichments found). **(E)** Expression patterns of
1175 bacterioferritin proteins in the extracellular vesicles of WT and *virR*^{mut}. **(F)** Expression
1176 patterns of proteins contributing to enrichments of terms related to mycolic acids
1177 biosynthesis. **(G)** Bottom left: Concentrations of key metabolites in the propionyl-coA
1178 detoxification routes. Right: Metabolic pathway of the propionyl-coA detoxification route
1179 through the methyl-malonyl route, along with the differential expression statistics
1180 between the WT and *virR*^{mut} strains observed at transcriptomic and proteomic levels for
1181 the main enzymes involved. The framed plot represents the quantification of selected
1182 metabolites by mass spectrometry.
1183
1184 **Figure 5. Cell permeability is a major driver of vesicle production in *Mtb*. (A)** Time
1185 course of the uptake of ethidium bromide (EthBr) by *Mtb* grown in the indicated
1186 conditions, as measured by fluorescence at 590 nm for 65 min. Data are mean and
1187 standard deviation of three biological replicates. **(B)** Dot-blot analysis of released EVs in
1188 supernatants from *Mtb* cultures submitted to the indicated conditions. The loading
1189 volume was normalized according to CFUs. The graph below represents the

1190 quantification of the dotblot using ImageJ. The integrated cell density was normalized
1191 WT values. Data are mean and standard errors from the three biological replicates; ****
1192 denotes P<0.0001, *** denotes P=0.0028 after applying a Tukey´s multiple comparison
1193 test. **(C)** Enrichment odds ratios for Fisher exact tests comparing sets of genes up, and
1194 down regulated, respectively, in 1)cholesterol-supplemented medium vs. glucose-
1195 supplemented medium ((Pawełczyk et al., 2021), GEO accession GSE175812); and 2)
1196 *virR*^{mut} vs WT. **(D)** Euler diagram showing that 39 out of 48 genes in the DosR regulon
1197 are simultaneously repressed in *virR*^{mut} vs WT, and upregulated in cholesterol vs.
1198 glucose enriched medium cultures, suggesting a common activation of the regulon in
1199 conditions of low permeability (see also Fig. S5). **(E)** Expression patterns in response to
1200 TRZ (1h) and in *virR*^{mut} for key genes involved in metal signaling, metabolism and
1201 homeostasis.
1202
1203 **Figure 6. Lipidomic analysis of cell envelope and EVs from *virR*^{mut}. (A)** Comparative
1204 total lipid analysis of the indicated strains by nano-LC-MS. Lipid species with an
1205 abundance higher than 0.5% are shown. Data indicates mean and standard error from
1206 three biological replicates. **(B)** Analysis of polar lipids of the indicated strains by
1207 bidimensional (2D)-layer chromatography (TLC) (2D-TLC). Phosphatidyl-myo-inositol
1208 dimannosides (Ac_1PIM_2 and Ac_2PIM_2, respectively); phosphatidyl-myo-inositol
1209 hexamannosides (Ac_xPIM_6); phosphatidylethanolamine (PE); diphosphatidylglycerol
1210 (DPG). Phospholipid (P). **(C)** Analysis of mycolic acid species in the indicated strains by
1211 TLC. **(D)** Analysis of PIDMs and TAGs by TLC. **(E)** Analysis of apolar lipids of the
1212 indicated strains by TLC. Diacylglycerol (DAG); free fatty acid (FF); free mycolic acid
1213 (FMA). **(F)** Analysis of apolar lipids of MEVs isolated from the indicated strains.
1214 Triacylglycerols (TAGs); phthiocerol dimycocerosates (PDIMs) **(G)** Analysis of polar
1215 lipids of MEVs isolated from the indicated strains. Phosphatidyl-myo-inositol
1216 dimannosides (Ac_1PIM_2 and Ac_2PIM_2, respectively); phosphatidyl-myo-inositol
1217 hexamannosides (Ac_xPIM_6); diphosphatidylglycerol (DPG).
1218
1219 **Figure 7. Chemical and nanometric analysis of isolated cell walls shows higher**
1220 **amounts of PG in the absence of VirR. (A)** Glycosyl composition analysis of isolated
1221 cell walls from the indicated strains. Acid hydrolysis prior to GC-MS analysis of isolated
1222 cell walls was performed to determine the total amounts of galactose (G), arabinose (A),
1223 rhamnose (R), and N-acetylglucosamine (NAGc). The ratio between different sugars is
1224 shown to indicate: (i) the relative levels of arabinogalactan (A/G); (ii) the length of the AG
1225 polysaccharide chain (G/R); (iii) the amount of PG (NAGc/Rham). Individual
1226 measurements are shown from three biological replicates. Data are mean and standard

1227 errors. **P < 0.01. **(B)** Quantification of diaminopimelic acid (DAP) on isolated cell walls
1228 from the indicated strains. Data are mean and standard errors from three biological
1229 replicates; **** denotes P<0.0001, * denotes P=0.0119 after applying a Tukey´s multiple
1230 comparison test. **(C)** Atomic force microscopy high resolution images taken in liquid from
1231 the external surface of purified peptidoglycan from different samples, left to right: WT,
1232 *virR*^{mut}, *virR*^{mut}*-C*, the structure of external peptidoglycan layer shows a mesh with pores
1233 of different sizes, **(D)** Graph showing the pore diameter from n = 8 AFM images similar
1234 to (**C**) (each point represent an image) of different samples; black triangles: WT, blue
1235 circles: *virR*^{mut}, green squares: *virR*^{mut}*-C*. The pore diameter was calculated from the
1236 binary slice from each image containing the greatest number of pores, according to
1237 (Pasquina-Lemonche, 2024). **(E)** The number of pores per surface area from different
1238 samples; white triangles: WT, red circles: *virR*^{mut}, blue squares: *virR*^{mut}-C, this was
1239 calculated from the slice containing the maximum number of pores where the pore size
1240 was analyzed, following the method from (Pasquina-Lemonche, 2024). **(F)** Graph
1241 showing the peptidoglycan thickness manually measured using the 1D statistic tools from
1242 the open-source program Gwyddion (Nečas and Klapetek, 2012) from AFM images in
1243 air containing several fragments of cell wall, each point represents a different
1244 peptidoglycan fragment from a different cell. There were three samples analyzed: white
1245 WT n=23 peptidoglycan fragments, red *virR*^{mut} n=36 and blue *virR*^{mut}-C n=25. Statistics:
1246 D) Using a two-tailed t test with Welch's correction the statistical comparison are: (***)
1247 pWT- *virR*^{mut} = 4.1 10-4 with t = 6.1, df = 7.5, (**) p *virR*^{mut} - *virR*^{mut}-C = 0.007 with t =
1248 3.2, df = 13.2, E) Using a two-tailed t test with Welch's correction the statistical
1249 comparison are: (****) pWT- *virR*^{mut} = 6.6 10-10 with t = 16.3, df = 12.7, (**) p *virR*^{mut} -
1250 *virR*^{mut} -C = 0.01 with t = 3.0, df = 13.2., F) Using a two-tailed t test with Welch's correction
1251 the statistical comparison are: (****) pWT- *virR*^{mut} = 2.8 10-18 with t = 17.8, df = 32.3,
1252 (****) *virR*^{mut} - *virR*^{mut} -C = 3.9 10-17 with t = 16.4, df = 31.8.
1253
1254 **Figure 8. VirR interacts with Lcp1. (A)** Blue-native PAGE analysis of recombinant VirR
1255 and Lcp1. The molecular mass of markers in kDa are indicated on the left side of the gel.
1256 The size of the multimers of VirR and Lcp1 are indicated on the left side of the gel. **(B)**
1257 *Upper panel*. Representative image of a flotation assay of recombinant VirR, Lcp1 and
1258 the mixture of both performed on an idioxanol density gradient. The presence of VirR or
1259 Lcp1 was detected in each fraction by dot-blot using murine polyclonal antibodies raised
1260 against VirR or Lcp1. Numbers indicate collected fractions from top (1) to bottom (11).
1261 *Lower panel*. Quantification of the dot-blot by measuring the pixel intensity of the dots
1262 using ImageJ. Data are mean and standard error of three independent experiments. **(C)**
1263 Bipartite split-GFP experiment using *M. smegmatis* D2 expressing plasmids depicted in

1264 *(C)*, including VirR, VirRsol(Δ1-41), $CtpC_N$, Rv3484, Rv3267 (Lcp1), Rv0822,
1265 $Rv3484_{LytR_C}$, $Rv3267_{LytR_C}$ and $Rv0822_{LytR_C}$. Bacteria were grown in complete 7H9.
1266 Fluorescence was recorded by epifluorescence microscopy. The experiment was
1267 performed one time.
1268
1269 **Supplementary Tables**
1270
1271 **Supplementary Table S1.** Plasmids and primers used in this study.

Construction / DNA fragment used	Template	Primers	Sequence 5'-3'
pGMCS-P1-*virR*-Lk2-GFP11-*ctpC*(1-85)-Lk15-GFP(1-10)			
P1	pGMCS-TetR-P1-*pacL1*$_{Flag}$- P$_{pacL1}$-*ctpC*$_{His}$ (Boudehen *et al*. 2022)	Inf-B2-P1-Fw	CAAAGTGGAGCGATACTCGACATCGGATCGTCGGCACCGTCAC
		Inf-P1-Left	GAAATGATGTATGCCGTGCTGGTC
pGMCS backbone	pGMCS-P$_{pacL}$-*pacL1*-Lk2-GFP11-*ctpC*(1-85)-Lk15-GFP(1-10) (Boudehen *et al*. 2022)	ctpC-B2-Left	GTCGAGTATCGCTCCACTTTG
		Rv3269-P1-Fus-Fw	CAGCACGGCATACATCATTTCGGAAGAAAGGTACAGGCAATGG
pGMCS-P1-*virR*-Lk2-GFP11-*ctpC*(1-85)-Lk15-GFP(1-10)			
virR	*M. tuberculosis* H37Rv chromosomal DNA	If-AmL1-VirR	AAGGTACAGGCAATGgtgctggttacagtgggctcg
		If-Lk2-VirR-Rv	ACCGGATCCTTCCAGgccggtcaccacgacgatg
pGMCS backbone	pGMCS-P1-*pacL1*-Lk2-GFP11-*ctpC*(1-85)-Lk15-GFP(1-10)	Lk2-Right	CTGGAAGGATCCGGTGGCGG
		pGMC 3269 Am Left	CATTGCCTGTACCTTTCTTCC
pGMCS-P1-*virRsol*-Lk2-GFP11-*ctpC*(1-85)-Lk15-GFP(1-10)			
virRsol	*M. tuberculosis* H37Rv chromosomal DNA	If-AmL1-VirRsol	AAGGTACAGGCAATGctgggttcgtctccgaactccg
		If-Lk2-VirR-Rv	ACCGGATCCTTCCAGgccggtcaccacgacgatg
pGMCS backbone	pGMCS-P1-*pacL1*-Lk2-GFP11-*ctpC*(1-85)-Lk15-GFP(1-10)	Lk2-Right	CTGGAAGGATCCGGTGGCGG
		pGMC 3269 Am Left	CATTGCCTGTACCTTTCTTCC
pGMCS-P1-*virR*-Lk2-GFP11-*virR*-Lk15-GFP(1-10)			
virR	*M. tuberculosis* H37Rv chromosomal DNA	If-AmMBD-VirR	GAGCGCCTCGCCATGgtgctggttacagtgggctcg
		If-L15-VirR-Rv	AGACAGCCCTGGACCgccggtcaccacgacgatg
pGMCS backbone	pGMCS-P1-*virR*-Lk2-GFP11-*ctpC*(1-85)-Lk15-GFP(1-10)	Flex15-Right	GGTCCAGGGCTGTCTGGCC
		ctpC-Am-left2	CATGGCGAGGCGCTCAAG
pGMCS-P1-*virRsol*-Lk2-GFP11-*virRsol*-Lk15-GFP(1-10)			
virRsol	*M. tuberculosis* H37Rv chromosomal DNA	If-AmMBD-VirRsol	GAGCGCCTCGCCATGctgggttcgtctccgaactccg
		If-L15-VirR-Rv	AGACAGCCCTGGACCgccggtcaccacgacgatg
pGMCS backbone	pGMCS-P1-*virRsol*-Lk2-GFP11-*ctpC*(1-85)-Lk15-GFP(1-10)	Flex15-Right	GGTCCAGGGCTGTCTGGCC
		ctpC-Am-left2	CATGGCGAGGCGCTCAAG
pGMCS-P1-*virRsol*-Lk2-GFP11-*rv0822c*(LytR_C)-Lk15-GFP(1-10)			
Rv0822c(LytR_C)	*M. tuberculosis* H37Rv chromosomal DNA	If-AmMBD-0822cD	GAGCGCCTCGCCATGgagattcagcaccagcaggttacgacg
		If-L15-0822cD-Rv	AGACAGCCCTGGACCgcggcttatctgcacgctgacg

pGMCS backbone	pGMCS-P1-*virRsol*-Lk2-GFP11-*ctpC*(1-85)-Lk15-GFP(1-10)	Flex15-Right	GGTCCAGGGCTGTCTGGCC
		ctpC-Am-left2	CATGGCGAGGCGCTCAAG
pGMCS-P1-*virRsol*-Lk2-GFP11-*rv3267*(LytR_C)-Lk15-GFP(1-10)			
Rv3267(LytR_C)	*M. tuberculosis* H37Rv chromosomal DNA	If-AmMBD-3267D	GAGCGCCTCGCCATGcccgccaagaccacggcc
		If-L15-3267D-Rv	AGACAGCCCTGGACCcagcccggagcccggac
pGMCS backbone	pGMCS-P1-*virRsol*-Lk2-GFP11-*ctpC*(1-85)-Lk15-GFP(1-10)	Flex15-Right	GGTCCAGGGCTGTCTGGCC
		ctpC-Am-left2	CATGGCGAGGCGCTCAAG
pGMCS-P1-*virRsol*-Lk2-GFP11-*rv3484*(LytR_C)-Lk15-GFP(1-10)			
Rv3484(LytR_C)	*M. tuberculosis* H37Rv chromosomal DNA	If-AmMBD-3484D	GAGCGCCTCGCCATGgcggccgccaaacctaacc
		If-L15-3484D-Rv	AGACAGCCCTGGACCggtatccaccgtcacacggatg
pGMCS backbone	pGMCS-P1-*virRsol*-Lk2-GFP11-*ctpC*(1-85)-Lk15-GFP(1-10)	Flex15-Right	GGTCCAGGGCTGTCTGGCC
		ctpC-Am-left2	CATGGCGAGGCGCTCAAG
pGMCS-P1-*virRsol*-Lk2-GFP11-*rv0822c*(Cterm)-Lk15-GFP(1-10)			
Rv0822c(Cterm)	*M. tuberculosis* H37Rv chromosomal DNA	If-AmMBD-0822cD	GAGCGCCTCGCCATGgagattcagcaccagcaggttacgacg
		If-L15-0822c-Rv2	AGACAGCCCTGGACCctcgcaggtggtgtcggcg
pGMCS backbone	pGMCS-P1-*virRsol*-Lk2-GFP11-*ctpC*(1-85)-Lk15-GFP(1-10)	Flex15-Right	GGTCCAGGGCTGTCTGGCC
		ctpC-Am-left2	CATGGCGAGGCGCTCAAG
pGMCS-P1-*virRsol*-Lk2-GFP11-*rv3267*(Cterm)-Lk15-GFP(1-10)			
Rv0822c(Cterm)	*M. tuberculosis* H37Rv chromosomal DNA	If-AmMBD-3267D	GAGCGCCTCGCCATGgagattcagcaccagcaggttacgacg
		If-L15-3267-Rv2	AGACAGCCCTGGACCgttgatgcactccggcgcgtc
pGMCS backbone	pGMCS-P1-*virRsol*-Lk2-GFP11-*ctpC*(1-85)-Lk15-GFP(1-10)	Flex15-Right	GGTCCAGGGCTGTCTGGCC
		ctpC-Am-left2	CATGGCGAGGCGCTCAAG
pGMCS-P1-*virRsol*-Lk2-GFP11-*rv3484*(Cterm)-Lk15-GFP(1-10)			
Rv0822c(Cterm)	*M. tuberculosis* H37Rv chromosomal DNA	If-AmMBD-3267D	GAGCGCCTCGCCATGgagattcagcaccagcaggttacgacg
		If-L15-3484-Rv2	AGACAGCCCTGGACCgttcacgcagggcacgccg
pGMCS backbone	pGMCS-P1-*virRsol*-Lk2-GFP11-*ctpC*(1-85)-Lk15-GFP(1-10)	Flex15-Right	GGTCCAGGGCTGTCTGGCC
		ctpC-Am-left2	CATGGCGAGGCGCTCAAG
pGMCS-P1-*virRsol*-Lk2-GFP11-*rv0822c*-Lk15-GFP(1-10)			
Rv0822c	*M. tuberculosis* H37Rv chromosomal DNA	If-AmMBD-0822c	GAGCGCCTCGCCATGagtgacggcgagagcg
		If-L15-0822c-Rv	AGACAGCCCTGGACCctactcgcaggtggtgtcgg
pGMCS backbone	pGMCS-P1-*virRsol*-Lk2-GFP11-*ctpC*(1-85)-Lk15-GFP(1-10)	Flex15-Right	GGTCCAGGGCTGTCTGGCC
		ctpC-Am-left2	CATGGCGAGGCGCTCAAG
pGMCS-P1-*virRsol*-Lk2-GFP11-*rv3267*-Lk15-GFP(1-10)			
Rv3267(Cterm)	*M. tuberculosis* H37Rv chromosomal DNA	If-AmMBD-3267	GAGCGCCTCGCCATGatgtctgcgcaacgtgtggttc
		If-L15-3267-Rv	AGACAGCCCTGGACCtcagttgatgcactccggcgc
pGMCS backbone	pGMCS-P1-*virRsol*-Lk2-GFP11-*ctpC*(1-85)-Lk15-GFP(1-10)	Flex15-Right	GGTCCAGGGCTGTCTGGCC
		ctpC-Am-left2	CATGGCGAGGCGCTCAAG
pGMCS-P1-*virRsol*-Lk2-GFP11-*rv3484*-Lk15-GFP(1-10)			

Rv3484(Cterm)	*M. tuberculosis* H37Rv chromosomal DNA	If-AmMBD-3484	GAGCGCCTCGCCATGgcgcgttctgagggc
		If-L15-3484-Rv	AGACAGCCCTGGACCctagttcacgcagggcacgc
pGMCS backbone	pGMCS-P1-*virRsol*-Lk2-GFP11-*ctpC*(1-85)-Lk15-GFP(1-10)	Flex15-Right	GGTCCAGGGCTGTCTGGCC
		ctpC-Am-left2	CATGGCGAGGCGCTCAAG
CRISPRi mutants			
virR (158.1) c2	Rv0431	Rv0431crispr 1 F	GGGAGAGCAGCAGGAAGACGACGC
		Rv0431crispr 1 R	AAACGCGTCGTCTTCCTGCTGCTC
virR (42.2) c1	Rv0431	Rv0431crispr 2 F	GGGAACGAACCCAGTGCCTGCCAGA
		Rv0431crispr 2 R	AAACTCTGGCAGGCACTGGGTTCGT
cei (145.2) c1	Rv2700	Rv2700crispr 1 F	GGGAATCACGCAAGTCACCACCAC
		Rv2700crispr 1 R	AAACGTGGTGGTGACTTGCGTGAT
cei (47.3) c2	Rv2700	Rv2700crispr 2 F	GGGAGTCGGTGCCGAGCGCAAGGTCG
		Rv2700crispr 2 R	AAACGACCTTGCGCTCGGCACCGAC
VirR-Venus primers			
VirR-F			TCACTGGGGTGCTGGTTACAGTGGGCTC
VirR-R			ATAGGATCGCCGGTCACCACGACGAT
pMV-F			TGACCGGCGATCCTATGGTGAGCAAGGGC
pMV-R			ACCAGCACCCCAGTGAAAAGTTCTTCTCCTTTACTC

Supplementary Table 2. Gradient mobile phase composition for ion-pairing LC-MS/MS for the quantification of acetyl-CoA, methyl citrate and methylmalonyl-CoA.

Time (min)	Mobile Phase (%)	
	A	B
1	100	0
2	55	45
7	50	50
7.5	5	95
8	5	95
8.5	100	0
10	End	

A: water-methanol 07:3 (v/v) + 10mM tributylamine + 3mM acetic acid; B: pure methanol

SupplementaryTable 3. Gradient mobile phase composition for ion-pairing LC-MS/MS for the quantification of pyruvate.

Time (min)	Mobile Phase (%)	
	A	B
1	5	95
6	95	5
7	95	5
8	5	95
10	End	

A: pure water; B: pure methanol

1282 **SupplementaryTable 4**. Quantifier MRM transitions and collision energies used
1283 for acety-CoA, methyl citrate, methylmalonyl-CoA and pyruvate.

Metabolite	Precursor ion $[M-H]^-$ (m/z)	Product ion (m/z)	Collision energy (eV)
Acetyl-CoA	808.00	407.95	41
Methyl citrate	204.90	125.10	13
Methylmalonyl-CoA	432.60	410.50	10
Pyruvate	87.20	43.10	13

1284
1285
1286
1287 **Supplementary figures**

1288 **Fig S1. Diversity of *Mtb* LCP proteins**. (**A**) Domain structure of LCP proteins in *Mtb*.
1289 Proteins are organized according to the presence of (i) both LCP (green) and LytR_C
1290 (slight orange) terminal domain (Rv3267, Rv3484 and Rv0822); (ii) the solo LytR_C
1291 domain (VirR and Rv2700); and the solo LCP domain (Rv3840). Additional information
1292 is provided for *Mtb* mutants in the indicated genes. (**B**) Phylogenetic analysis of LCP
1293 proteins in Mycobacteria (*M. tuberculosis, M. smegmatis, M. marinum and M. leprae*).
1294 The unrooted tree includes seven separate clusters for proteins with both LCP and
1295 LytR_C terminal domains (CpsA1, CpsA2 and CpsA3); with the solo LytR_C terminal
1296 domain (Solo_LytRC1 and Solo_LytRC2); with the solo LCP domain; and a separate
1297 cluster including the characterized LCP proteins from *S. pneumonia* and *S. aureus*. Note
1298 the clustering of one of the *M. smegmatis* LCP proteins with this group. VirR is highlighted
1299 in blue.
1300

1301 **Fig S2. The enhanced vesiculation phenotype of *virR*^{mut} occurs in the absence of**
1302 **cell lysis**. **(A)** Nanoparticle tracking analysis (NTA) of EV preparations derived from WT
1303 and the indicated strains showing number of particles per cm^3 determined by Zeta View
1304 NTA in three independent EV preparations. Data are presented as mean ± SEM.
1305 *$P \leq 0.05$ (One-way ANOVA with Tukey's multiple comparisons test). **(B)** Cell lysis
1306 control of *virRmut*. Shown are immunoblots of cell lysates and culture supernatants (SN)
1307 for the indicated strains. The cytoplasmic protein IdeR was detected in cell lysates but
1308 not in culture supernatants confirming cell integrity, while the secreted protein Ag85b
1309 was readily detected in the culture supernatants. **(C)** Cell lysis control of *Mtb* submitted
1310 to conditions that alter permeability. Arrows indicate the size of the proteins of interest
1311 detected by immunoblot.
1312

1313 **Fig S3. Expression patterns of proteins contributing to enrichments of terms**
1314 **related to translation.**
1315

1316 **Fig S4. Expression patterns of proteins contributing to enrichments of terms**
1317 **related to nucleotide (A), amino-acids (B), oligosaccharides (C), and glycogen (D)**
1318 **metabolism, differentially expressed in both directions.**
1319
1320 **Fig S5. Expression patterns of the 39 genes in the DosR regulon that are**
1321 **simultaneously upregulated in cholesterol-enriched medium and down-regulated**
1322 **in *virR*^{mut} (Pawełczyk et al., 2021, GSE175812).**
1323
1324 **Fig S6. Additional AFM data. (A-C) (i)** Atomic force microscopy images taken in liquid
1325 from a big area showing the sample heterogeneity overview with various peptidoglycan
1326 fragments of the following samples: **(A)** WT, **(B)** *virR*^{mut}, **(C)**, *virR*^{mut}-C. **(ii)** Atomic force
1327 microscopy images zoom in one individual peptidoglycan fragment corresponding to one
1328 cell from different samples: **(A)** WT, **(B)** *virR*^{mut} showing the background (Backg.), the
1329 external surface (Ext) the internal (Int), **(C)**, *virR*^{mut}-C, white square showing the size of
1330 the zoom images shown in Figure 5 from the external surface of the cells. **(D)** Curve of
1331 grey points showing 255 slices of one AFM image taken using the FIJI macro presented
1332 in (Pasquina-Lemonche, 2024), in the x axis and the total number of pores in the y axis,
1333 the red line is a Gaussian fitted to the curve and the maximum of the Gaussian is marked
1334 with a dash red line showing slice 140 in this example corresponding to the slice of the
1335 image with the maximum number of pores. **(E)** Binary slice number 140 from the original
1336 AFM image showing the pores in white and the material represented in black. **(F)** The
1337 pores from 'E' were analyzed using the FIJI macros shown in (Pasquina-Lemonche,
1338 2024) where each pore area was measured and plotted in the x axis against the
1339 cumulative fraction of total pore area in the y axis as shown in the curve by blue dots.
1340 The red dot marks the most likely pore area which corresponds to the half of the
1341 cumulative fraction of the total pore area, this area was then used to obtain the pore
1342 diameter of the image. The same was repeated with the n = 8 images for each sample
1343 to compose the graphs 'D' and 'E' from Figure 7.
1344
1345 **Fig S7**. **Sensitivity to lysozyme of *virR*^{mut}.** **(A)** Analysis of the minimum inhibitory
1346 concentration (MIC) of lysozyme of the indicated strains by the resazurin method. **(B)**
1347 Growth of WT and *virR*^{mut} treated with 0 or 50 µl/mL lysozyme (Lys). Data represents the
1348 mean ± SEM of three independent cultures.
1349
1350 **Fig S8. Localization of VirR by fluorescence microscopy**. Fluorescence images of a
1351 *Mtb* strain expressing Venus-tagged VirR.
1352

1353 **Fig S9. Split-GFP strategy. (A)** *Upper panel*. Scheme of the plasmid used to test VirR
1354 interactions in vivo. *Lower panel*. Scheme of the potential molecular interaction between
1355 VirR and Lcp1 using split-GFP. **(B)** Gating strategy to analyze split-GFP flow cytometry
1356 data. Bacteria were first sorted based on size (FSC) and structure (SSC) to exclude
1357 debris (1). Then, aggregates were excluded based on FSC and SSC width (W) and
1358 eighth (H) (2,3). GFP signal was then analyzed *vs*. SSC (4) or mCherry, when relevant
1359 (5).
1360
1361
1362

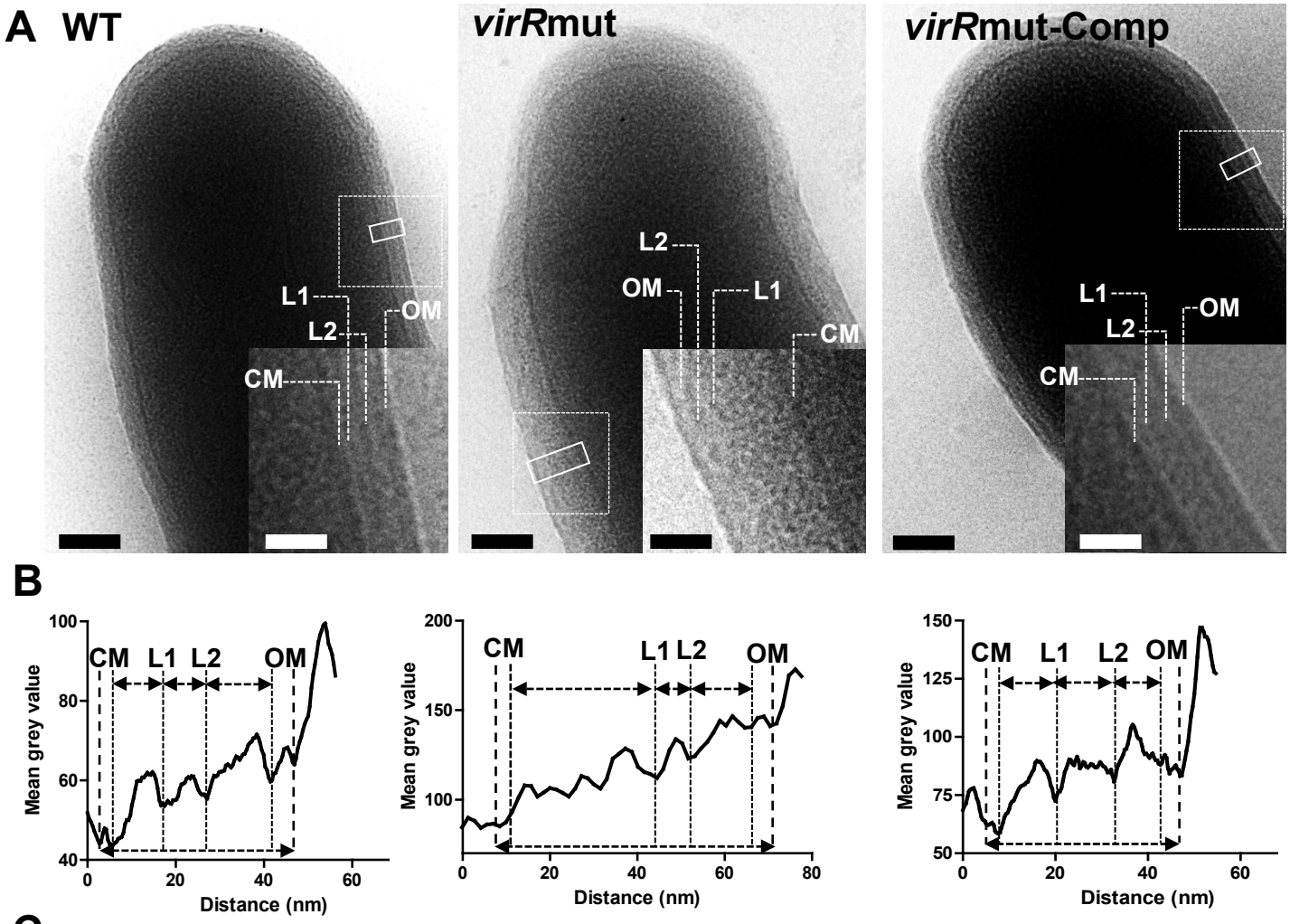

C

	CM	CM-OM	CM-L1	OM-L2	L1-L2	OM
WT	2.7±0.2	44.09±3.1	11.2±0.4	13.34±0.9	10.46±1.4	5.7±0.4
***virR* mut**	5.4±0.7*	62.7±3.2*	31.36±3.2*	15.1±2.2	6.8±0.9*	6.1±0.3
***virR* mut-Comp**	2.5±0.5	41.6±0.7	12.4±1.4	10.03±1.1	12.6±1.3	5±0.2

Figure 1

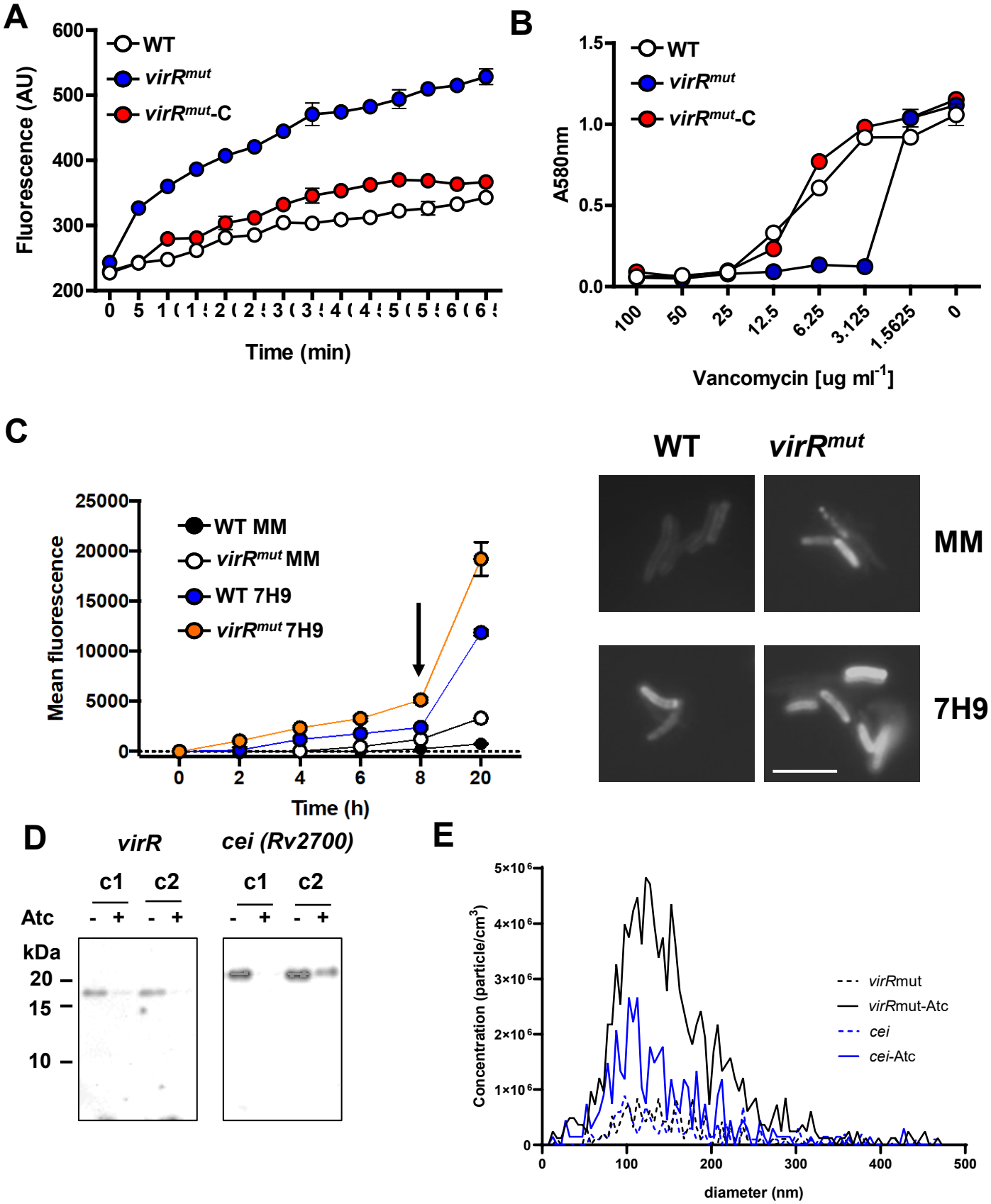
A
Fluorescence (AU)
600
500
400
300
200
WT
virRmut
virRmut-C
Time (min)
B
A580nm
1.5
1.0
0.5
0.0
WT
virRmut
virRmut-C
100
50
25
12.5
6.25
3.125
1.5625
0
Vancomycin [ug ml-1]
C
Mean fluorescence
25000
20000
15000
10000
5000
0
WT MM
virRmut MM
WT 7H9
virRmut 7H9
0
2
4
6
8
20
Time (h)
WT
virRmut
MM
7H9
D
virR
cei (Rv2700)
c1
c2
c1
c2
Atc
- + - +
- + - +
kDa
20
15
10
E
Concentration (particle/cm3)
5×10 6
4×10 6
3×10 6
2×10 6
1×10 6
0
virRmut
virRmut-Atc
cei
cei-Atc
0
100
200
300
400
500
diameter (nm)

Figure 2

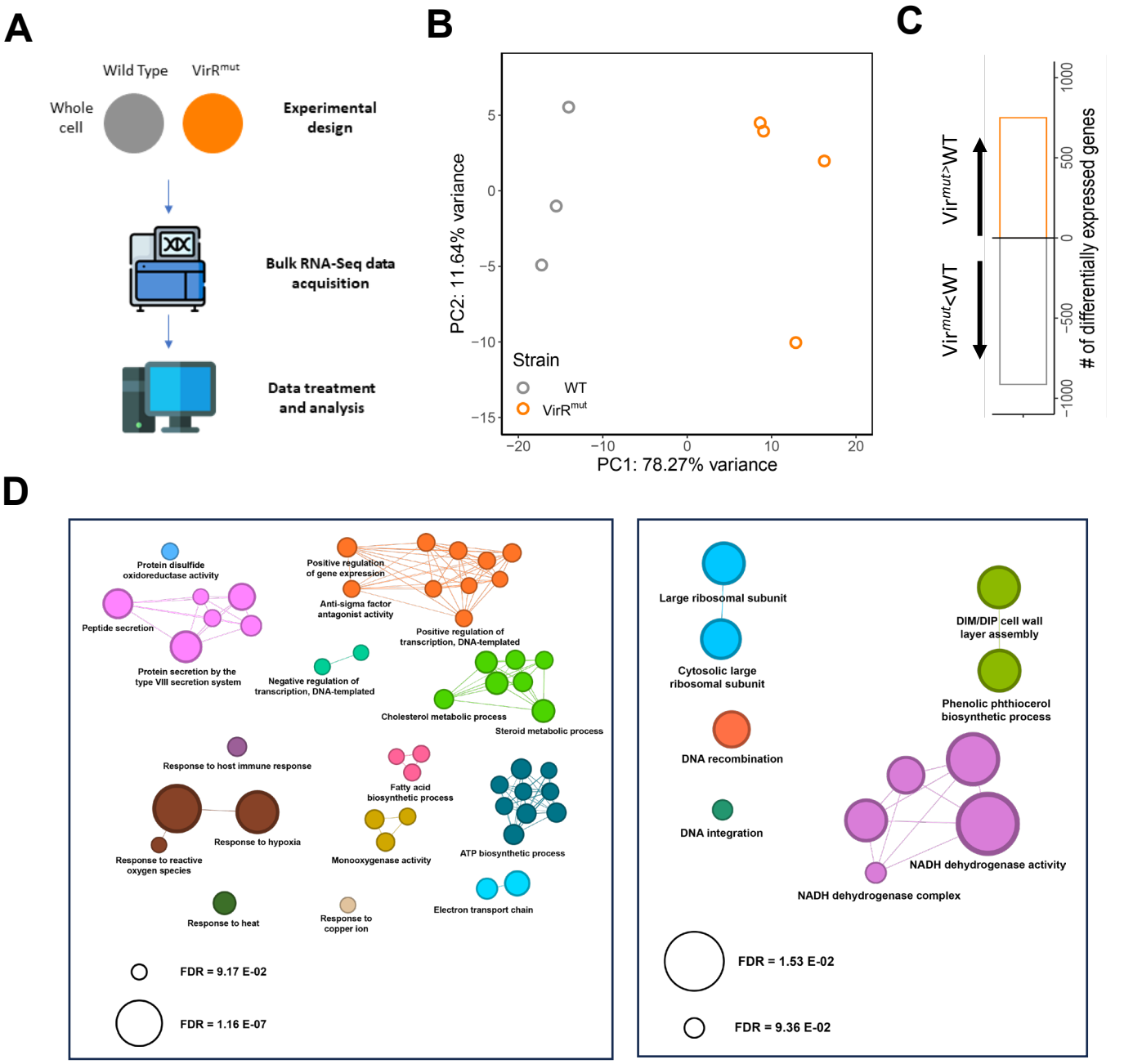
A
Wild Type
VirR^mut
Whole cell
Experimental design
Bulk RNA-Seq data acquisition
Data treatment and analysis
B
PC2: 11.64% variance
PC1: 78.27% variance
Strain
WT
VirR^mut
C
Vir^mut>WT
Vir^mut<WT
# of differentially expressed genes
D
Protein disulfide oxidoreductase activity
Peptide secretion
Protein secretion by the type VIII secretion system
Positive regulation of gene expression
Anti-sigma factor antagonist activity
Positive regulation of transcription, DNA-templated
Negative regulation of transcription, DNA-templated
Cholesterol metabolic process
Steroid metabolic process
Response to host immune response
Response to hypoxia
Response to reactive oxygen species
Fatty acid biosynthetic process
Monooxygenase activity
ATP biosynthetic process
Electron transport chain
Response to heat
Response to copper ion
FDR = 9.17 E-02
FDR = 1.16 E-07
Large ribosomal subunit
Cytosolic large ribosomal subunit
DNA recombination
DNA integration
DIM/DIP cell wall layer assembly
Phenolic phthiocerol biosynthetic process
NADH dehydrogenase activity
NADH dehydrogenase complex
FDR = 1.53 E-02
FDR = 9.36 E-02

Figure 3

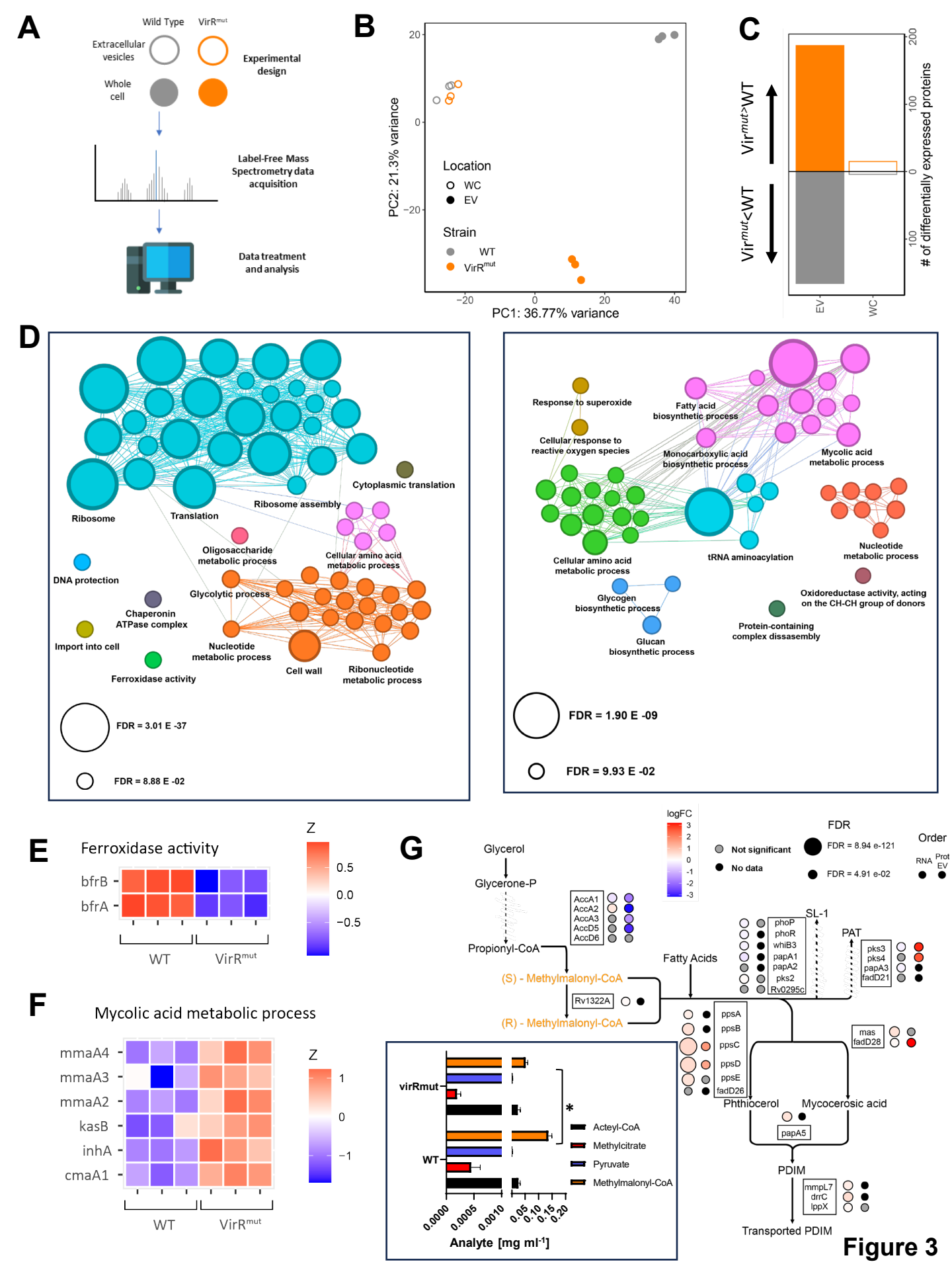
A
Wild Type
VirR^mut
Extracellular vesicles
Whole cell
Experimental design
Label-Free Mass Spectrometry data acquisition
Data treatment and analysis
B
PC2: 21.3% variance
PC1: 36.77% variance
Location
WC
EV
Strain
WT
VirR^mut
C
Vir^mut>WT
Vir^mut<WT
# of differentially expressed proteins
EV
WC
D
Ribosome
Translation
Ribosome assembly
Cytoplasmic translation
Oligosaccharide metabolic process
Cellular amino acid metabolic process
DNA protection
Glycolytic process
Chaperonin ATPase complex
Import into cell
Nucleotide metabolic process
Cell wall
Ribonucleotide metabolic process
Ferroxidase activity
FDR = 3.01 E -37
FDR = 8.88 E -02
Response to superoxide
Fatty acid biosynthetic process
Cellular response to reactive oxygen species
Monocarboxylic acid biosynthetic process
Mycolic acid metabolic process
Nucleotide metabolic process
Cellular amino acid metabolic process
tRNA aminoacylation
Oxidoreductase activity, acting on the CH-CH group of donors
Glycogen biosynthetic process
Protein-containing complex dissassembly
Glucan biosynthetic process
FDR = 1.90 E -09
FDR = 9.93 E -02
E
Ferroxidase activity
bfrB
bfrA
WT
VirR^mut
Z
F
Mycolic acid metabolic process
mmaA4
mmaA3
mmaA2
kasB
inhA
cmaA1
WT
VirR^mut
Z
G
Glycerol
Glycerone-P
Propionyl-CoA
(S) - Methylmalonyl-CoA
(R) - Methylmalonyl-CoA
Rv1322A
AccA1
AccA2
AccA3
AccD5
AccD6
logFC
Not significant
No data
FDR
FDR = 8.94 e-121
FDR = 4.91 e-02
Order
RNA
Prot
EV
Fatty Acids
phoP
phoR
whiB3
papA1
papA2
pks2
Rv0295c
SL-1
PAT
pks3
pks4
papA3
fadD21
ppsA
ppsB
ppsC
ppsD
ppsE
fadD26
mas
fadD28
Phthiocerol
Mycocerosic acid
papA5
PDIM
mmpL7
drrC
lppX
Transported PDIM
virRmut
WT
Acteyl-CoA
Methylcitrate
Pyruvate
Methylmalonyl-CoA
Analyte [mg ml-1]

Figure 3

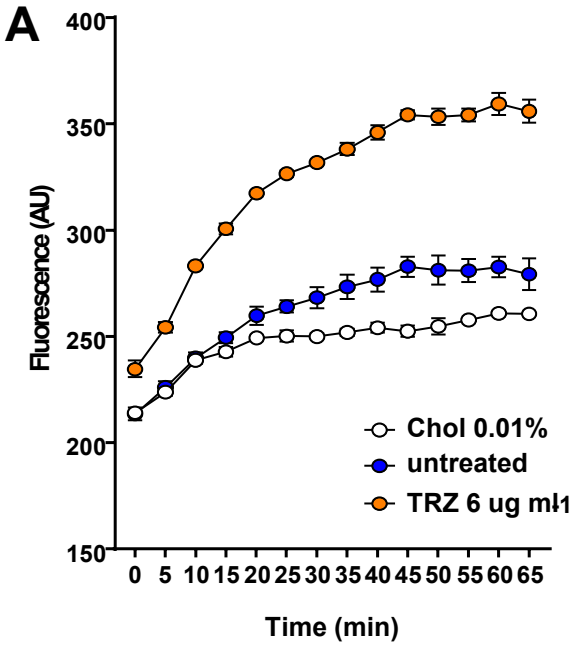
A
Fluorescence (AU)
Time (min)
Chol 0.01%
untreated
TRZ 6 ug ml-1

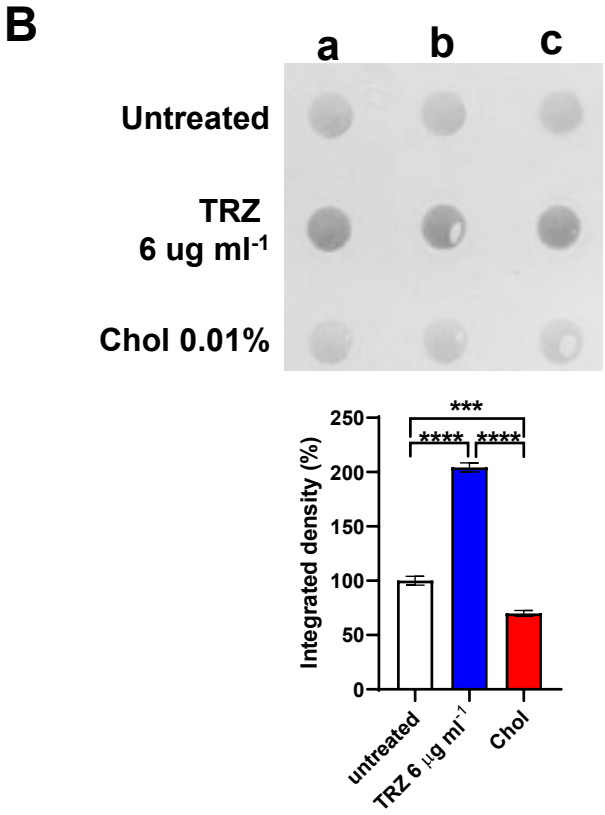
B
a
b
c
Untreated
TRZ
6 ug ml-1
Chol 0.01%
Integrated density (%)
untreated
TRZ 6 µg ml-1
Chol

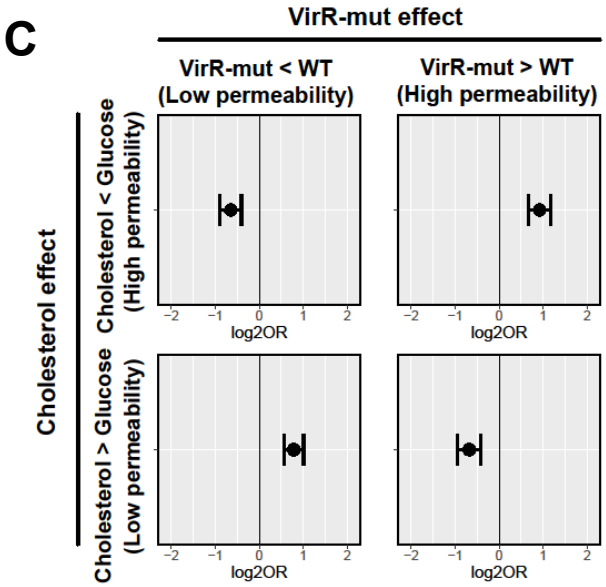
C
VirR-mut effect
VirR-mut < WT
(Low permeability)
VirR-mut > WT
(High permeability)
Cholesterol effect
Cholesterol < Glucose
(High permeability)
Cholesterol > Glucose
(Low permeability)
log2OR

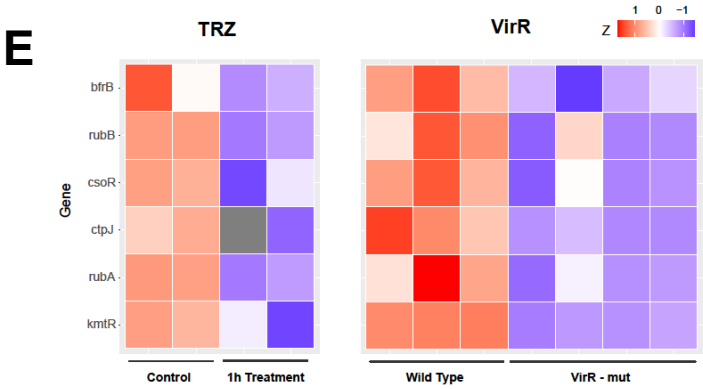
E
TRZ
VirR
Gene
bfrB
rubB
csoR
ctpJ
rubA
kmtR
Control
1h Treatment
Wild Type
VirR - mut

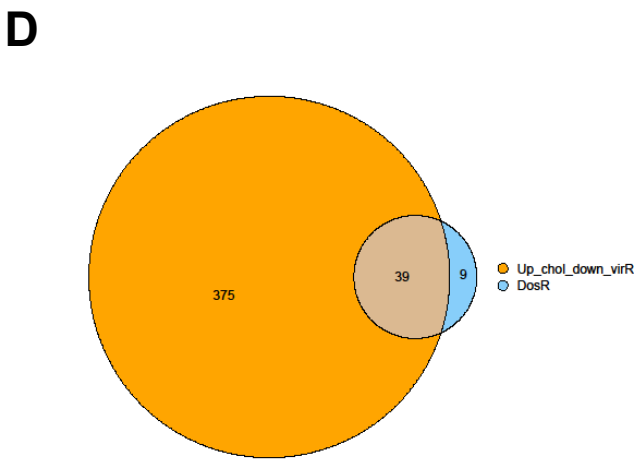
D
375
39
9
Up_chol_down_virR
DosR

Figure 5

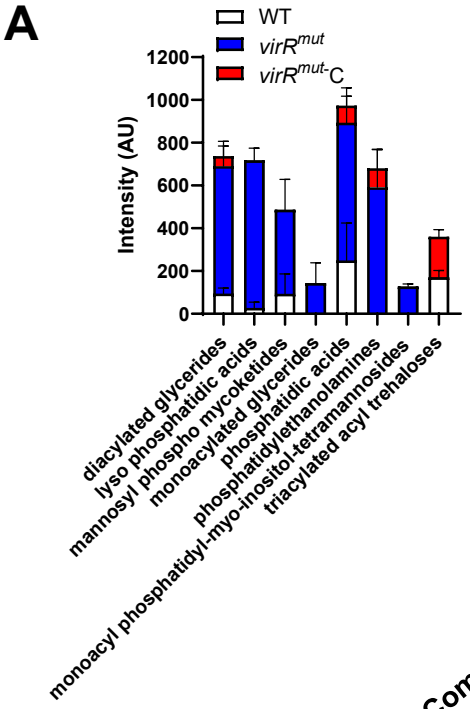
A
WT
virRmut
virRmut-C
Intensity (AU)
1200
1000
800
600
400
200
0
diacylated glycerides
lyso phosphatidic acids
mannosyl phospho mycoketides
monoacylated glycerides
phosphatidic acids
phosphatidylethanolamines
monoacyl phosphatidyl-myo-inositol-tetramannosides
triacylated acyl trehaloses

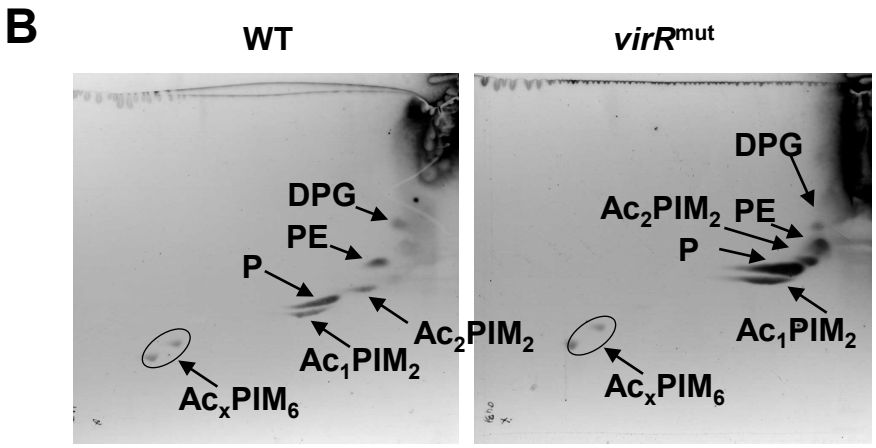
B
WT
virRmut
DPG
PE
P
Ac2PIM2
Ac1PIM2
AcxPIM6
DPG
Ac2PIM2
PE
P
Ac1PIM2
AcxPIM6

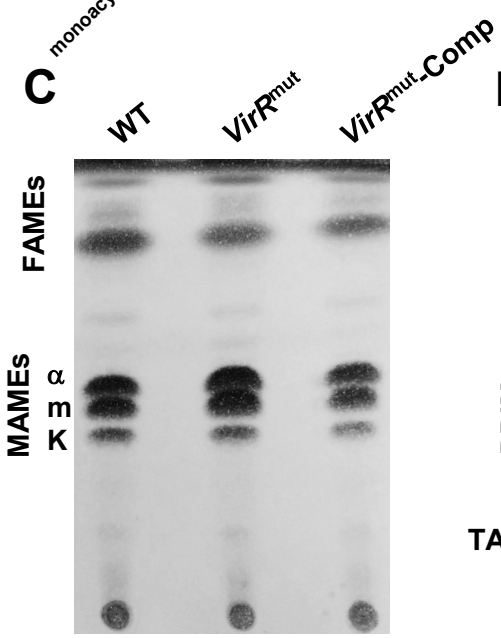
C
WT
VirRmut
VirRmut-Comp
FAMEs
MAMEs
α
m
K

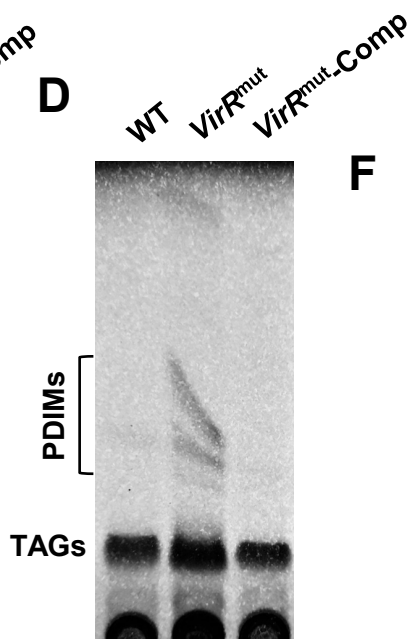
D
WT
VirRmut
VirRmut-Comp
PDIMs
TAGs

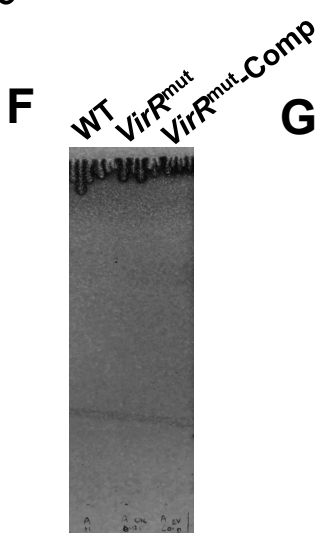
F
WT
VirRmut
VirRmut-Comp

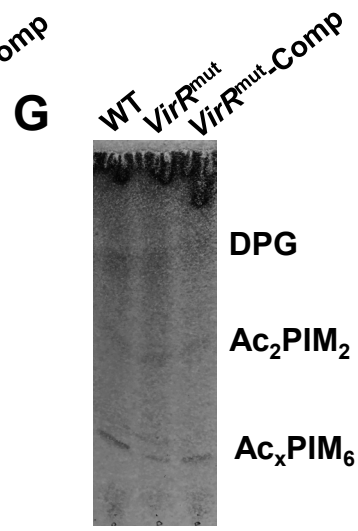
G
WT
VirRmut
VirRmut-Comp
DPG
Ac2PIM2
AcxPIM6

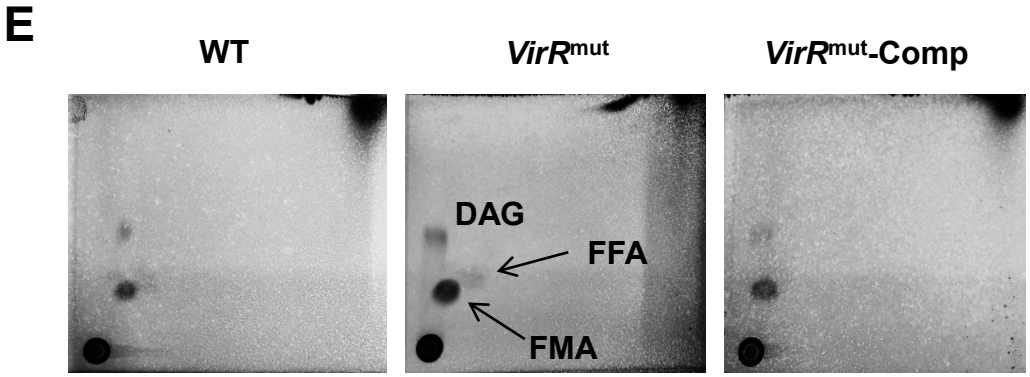
E
WT
VirRmut
VirRmut-Comp
DAG
FFA
FMA

Figure 6

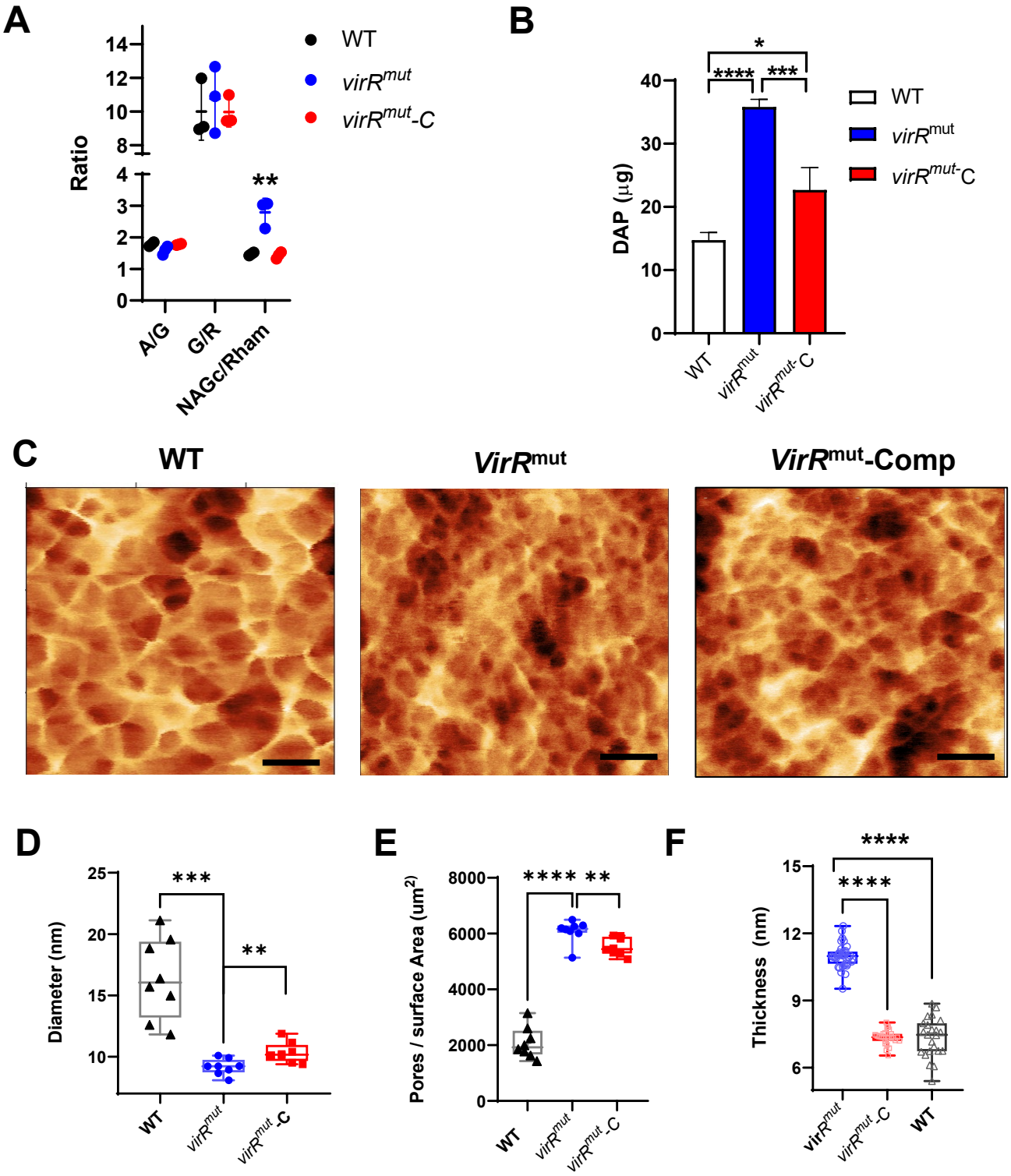
A
Ratio
WT
virRmut
virRmut-C
**
A/G
G/R
NAGc/Rham
B
DAP (µg)
*
****
***
WT
virRmut
virRmut-C
C
WT
VirRmut
VirRmut-Comp
D
Diameter (nm)
***
**
E
Pores / surface Area (um2)
**** **
F
Thickness (nm)
****
****

Figure 7

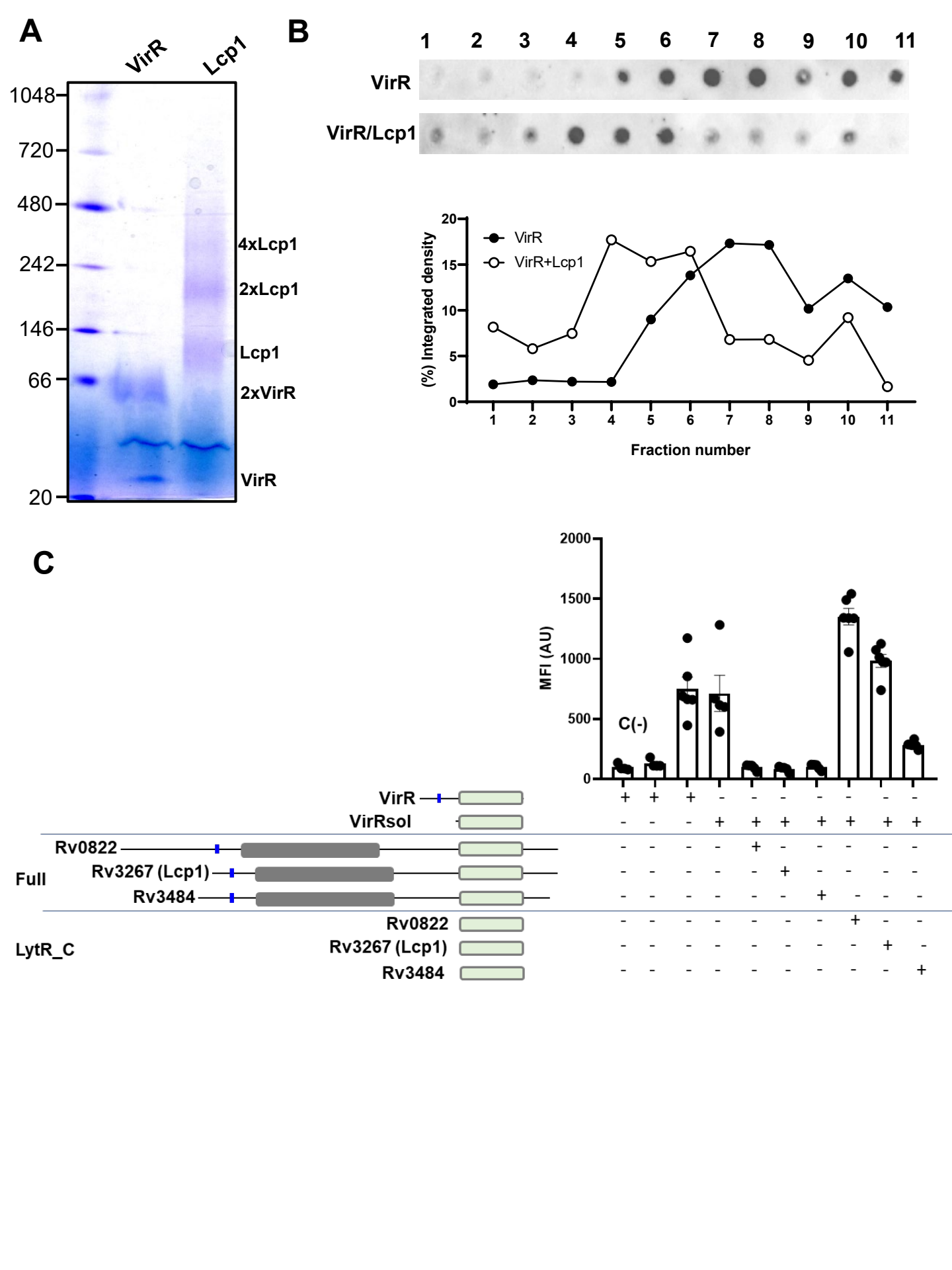
A
VirR
Lcp1
1048
720
480
242
146
66
20
4xLcp1
2xLcp1
Lcp1
2xVirR
VirR
B
1 2 3 4 5 6 7 8 9 10 11
VirR
VirR/Lcp1
(%) Integrated density
VirR
VirR+Lcp1
Fraction number
C
MFI (AU)
C(-)
VirR
VirRsol
Rv0822
Rv3267 (Lcp1)
Rv3484
Full
Rv0822
Rv3267 (Lcp1)
Rv3484
LytR_C